

# Turbulence in simulated HII regions

S.-N. X. **Medina**<sup>1,2</sup>, S. J. Arthur<sup>2,4</sup>\*, W. J. Henney<sup>2,4</sup>, G. Mellema<sup>3,4</sup>, A. Gazol<sup>2</sup>

<sup>1</sup>*Departamento de Astronomía, Universidad de Guanajuato, Guanajuato, México.*

<sup>2</sup>*Centro de Radioastronomía y Astrofísica, Universidad Nacional Autónoma de México, Campus Morelia, 58090 Morelia, Michoacán, México.*

<sup>3</sup>*Dept. of Astronomy and Oskar Klein Centre, AlbaNova, Stockholm University, SE-106 91 Stockholm, Sweden.*

<sup>4</sup>*Nordita, KTH Royal Institute of Technology and Stockholm University, Roslagstullsbacken 23, SE-106 91 Stockholm, Sweden.*

## ABSTRACT

We investigate the scale dependence of fluctuations inside a realistic model of an evolving turbulent HII region and to what extent these may be studied observationally. We find that the multiple scales of energy injection from champagne flows and the photoionization of clumps and filaments leads to a flatter spectrum of fluctuations than would be expected from top-down turbulence driven at the largest scales. The traditional structure function approach to the observational study of velocity fluctuations is shown to be incapable of reliably determining the velocity power spectrum of our simulation. We find that a more promising approach is the Velocity Channel Analysis technique of Lazarian & Pogosyan (2000), which, despite being intrinsically limited by thermal broadening, can successfully recover the logarithmic slope of the velocity power spectrum to a precision of  $\pm 0.1$  from high resolution optical emission line spectroscopy.

**Key words:** hydrodynamics — HII regions — ISM: kinematics and dynamics — turbulence

## 1 INTRODUCTION

The line broadening in excess of thermal broadening seen in optical spectroscopic studies of HII regions has been attributed to turbulence in the photoionized gas. There are many examples in the literature of attempts to identify the presence and characterize this turbulence, for example Münch (1958), Roy & Joncas (1985), O’Dell & Castañeda (1987), Miville-Deschênes, Joncas, & Durand (1995), Medina Tanco et al. (1997), Lagrois & Joncas (2011) and references cited by these papers. In these studies, the variation of the point-to-point radial velocities with scale was investigated using structure functions following von Hoerner (1951).

A general finding of these studies is that the structure function derived from these observations does not follow that predicted by Kolmogorov’s law (Kolmogorov 1941). The interpretation of this result is that Kolmogorov’s law for incompressible and subsonic turbulent flows cannot be strictly applied to the photoionized gas in HII regions, which will be compressible and possibly mildly supersonic (Roy & Joncas 1985), or that energy does not cascade from larger to smaller scales but is input at many scales (Castañeda 1988). Moreover, the results differ according to which emission lines are used in the study, since the topology of the emitting gas will be different. For instance, the [O III] $\lambda 5007$  line comes from

gas in the interior of an HII region, whereas the [S II] $\lambda 6731$  line comes from the vicinity of the ionization front, essentially a two-dimensional surface. The suggested mechanisms responsible for the generation and maintenance of the turbulent velocities in HII regions include photoevaporated flows from globules (Dyson 1968; O’Dell & Castañeda 1987) and stellar winds (Medina Tanco et al. 1997; Lagrois & Joncas 2011).

In order to construct the structure functions for the velocity fields, observations at many points in an HII region are needed. This can be achieved either by multiple longslit spectroscopic observations at many positions across a nebula (O’Dell, Townsley, & Castañeda 1987; Castañeda & O’Dell 1987; Wen & O’Dell 1993), or by Fabry-Perot interferometry (Roy & Joncas 1985; Miville-Deschênes, Joncas, & Durand 1995; Lagrois et al. 2011). Longslit observations with high velocity resolution have enabled several velocity components to be identified for emission lines of metal ions for which the thermal widths are small, e.g., [O III] $\lambda 5007$ . These observations have been used to determine the radial velocities of the principal components of the emitting gas at hundreds of positions within the nebula. Fabry-Perot observations produce datasets of thousands of radial velocities, but without the velocity resolution to distinguish between different velocity components. Obviously, in order to obtain a structure function over a wide range of scales, very high quality data with an ample spatial coverage are required. In the case of longslit spectra, this is a non-trivial task, not least the cali-

\* E-mail: j.arthur@crya.unam.mx

brating of the positions of the slits (García-Díaz & Henney 2007; García-Díaz et al. 2008).

Chandrasekhar (1949) suggested that turbulence is ubiquitous in astrophysics and that it could be analysed statistically via the spectrum of the velocity field, which expresses the correlations between instantaneous velocity components at all possible pairs of points in the medium. Turbulence develops in a fluid when velocity advection is dominant over dissipation (high Reynolds number), then continuous injection of energy is required in order to maintain the turbulent state. One of the main assumptions of the Kolmogorov theory of turbulence is that energy is only injected at large scales and is dissipated only at small scales. This implies that the energy cascades from large to small scales without dissipation. Another assumption of this theory is that in the range between injection and dissipation scales the energy is transferred at a constant rate, and this range is called the inertial range. Turbulence is often described in terms of the energy spectrum  $E(v)$ , and the inertial range is represented by a power-law relationship  $E(v) \propto k^\beta$ , where  $k$  is the wave number. For incompressible, homogeneous, isotropic, 3D turbulence (Kolmogorov 1941), we have  $\beta = -5/3$ , while in the limit of high Mach number, shock-dominated turbulence in one dimension (Burgers 1974), the power law is  $\beta = -2$ . It has proved more difficult to obtain exact results for the general case of 3D compressible, hydrodynamic turbulence. Scaling laws suggest that the original Kolmogorov energy spectrum scaling should be preserved even for highly compressible turbulence if the density weighted velocity  $\rho^{1/3}v$  is taken instead of the pure velocity  $v$  (Kritsuk et al. 2007; Federrath et al. 2010). Recent work by Galtier & Banerjee (2011) predicts the relation  $E(\rho^{1/3}v) \propto k^{-19/9}$  for compressible, isothermal turbulence with compressive driving, with a turnover around the sonic scale to  $E(\rho^{1/3}v) \propto k^{-5/3}$ . This has been confirmed by extremely high resolution numerical experiments (Federrath 2013).

Another important prediction of the Kolmogorov theory is the scaling of the structure function of any order. The universality of such scaling laws has been tested by detailed numerical experiments (Porter, Pouquet, & Woodward 2002; Boldyrev, Nordlund, & Padoan 2002; Kritsuk et al. 2007; Federrath 2013). Even in numerical experiments of incompressible, homogeneous and isotropic turbulence with energy injection at a fixed large scale, it is found that the exponents of the higher order structure functions have an anomalous behaviour, which has been interpreted as the result of spatial and/or temporal intermittency. Intermittency is a sparseness in space and time of strong structures associated with the dissipation or injection of energy (She & Leveque 1994). Since astrophysical turbulence driven by real physical phenomena is almost certainly intermittent, it is important to understand the possible effects of intermittency on the derived statistical properties of real H II regions.

The three-dimensional properties of the density and velocity fields that describe the turbulence in the interstellar medium, in this case an H II region, must be deduced from the statistical properties of the observed quantities. For photoionized gas, the observations generally consist of spectra at different positions, from which centroid velocities and linewidths can be obtained. For optical line emission, the emissivity depends on density, temperature and ionization

state and therefore an analysis of the emission lines will not just be providing information on the turbulent velocity fluctuations in the gas. The observations are a two-dimensional projection of the three-dimensional properties and much effort has been dedicated to the problem of recovering 3D information from 2D data (Lazarian & Pogosyan 2000; Brunt & Heyer 2002; Miville-Deschênes, Levrier, & Falgarone 2003; Brunt & Mac Low 2004; Esquivel & Lazarian 2005; Brunt, Federrath, & Price 2010). Generally, some simplifying assumptions, such as isothermal gas and statistical isotropy of the turbulence, must be made.

Recent modeling of H II regions has addressed the origin of the irregular structures, filaments, and globules seen within and around the borders in optical images (García-Segura & Franco 1996; Williams, Ward-Thompson, & Whitworth 2001; Mellema et al. 2006a; Mackey & Lim 2010; Arthur et al. 2011). Morphologically, the simulated emission-line images are very reminiscent of observed H II regions and the global dynamics, as measured by the r.m.s. velocity, is also similar to observationally derived values (García-Díaz et al. 2008; Arthur et al. 2011; Lagrois et al. 2011). The internal dynamics of the simulated H II regions is due mainly to the interaction of photoevaporated flows from the heads of the filaments and clumps, which flow into the interior of the H II region, superimposed on the general expansion of the H II region (Mellema et al. 2006a; Lagrois et al. 2011). However, the dynamics of real H II regions could also be affected at large scales by the action of stellar winds from the ionizing star or stars, and at small scales by outflows from young, low-mass stars.

In this paper we investigate to what extent our numerical simulations of H II regions model observed statistical properties of real H II regions. In § 2 we briefly describe the numerical methods used in the radiation-hydrodynamics simulations and in the calculation of the simulated emission-line radiation, and how the statistical information is obtained from these calculations. In § 3 we describe our results for the expansion of an H II region in a turbulent, clumpy molecular cloud. We discuss these results in § 4, and comment on the extent to which the statistical properties of the numerical simulations agree with those of observed H II regions. In § 5 we summarize and present our conclusions.

## 2 NUMERICAL MODEL

We perform radiation-hydrodynamic simulations of the expansion of photoionized regions in a non-uniform initially neutral medium. The central ionizing source has an effective temperature of 37,500 K and an ionizing photon rate of  $10^{48.5} \text{ s}^{-1}$ , which corresponds approximately to an O7 star.

The simulation takes as an initial condition a clumpy medium with mean density  $\langle n_0 \rangle = 1000 \text{ cm}^{-3}$ , which results from a self-gravitating forced turbulence simulation by Vázquez-Semadeni, Kim, & Ballesteros-Paredes (2005). The computational cube represents a spatial volume of  $4 \text{ pc}^3$  and the initial temperature is 5 K.

The radiation-hydrodynamics code used in the present paper does not include self gravity. However, on the relatively short timescales of the simulations ( $\sim 3 \times 10^5 \text{ yrs}$ ) this will not be important since the global free-fall time of the computational cube is  $\sim 6 \times 10^5 \text{ yrs}$ .

## 2.1 Radiation-hydrodynamics Code

The radiation-hydrodynamics code used in this paper is the same as that used by Mellema et al. (2006a). The hydrodynamics is calculated using the nonrelativistic Roe solver PPM scheme described in Eulderink & Mellema (1995) with the addition of a local oscillation filter (Sutherland, Bisset, & Bicknell 2003) to suppress numerical odd-even decoupling behind radiatively cooling shock waves. Heating and cooling in the ionized and neutral gas is dealt with in the same manner as described in detail by Henney et al. (2009). The radiation transport and photoionization makes use of the C<sup>2</sup>-RAY (Conservative-Causal ray) code developed by Mellema et al. (2006b). The calculations are all performed on a fixed, uniform Cartesian grid in three dimensions with a resolution of  $512^3$  cells.

## 2.2 Simulated Emission Lines

The emissivity cubes for the H $\alpha$  recombination line and the [O III] $\lambda$ 5007, [N II] $\lambda$ 6584 and [S II] $\lambda$ 6731 collisionally excited lines are calculated as described in Arthur et al. (2011), with the assumption that the heavy element ionization fractions are fixed functions of the hydrogen ionization fractions, calibrated with the Cloudy photoionization code.

## 2.3 Turbulence Statistics

The emissivity statistics have contributions from velocity, density, temperature and ionization state fluctuations. Obviously, the velocity fluctuations are the most dynamically important statistic and spectral line data, both real and simulated, can be used to extract statistical information for the different contributions. In particular, the second-order structure function of the velocity centroids and the technique of velocity-channel analysis (VCA; Lazarian & Pogosyan 2000) have been widely used.

In this paper, we calculate the second-order structure function of the velocity centroids of the simulated emission lines and also apply VCA to the corresponding position-position-velocity (PPV) datacubes. In addition, we calculate the power spectrum of the velocity field, both weighted and unweighted, of the 3D hydrodynamic simulation datacube in an attempt to relate the observed statistics to the underlying hydrodynamics.

### 2.3.1 Power Spectrum

The power spectrum is a statistical tool that is useful for describing the intrinsic properties of, for example, velocity and density fields or any other physical property. It is the Fourier transform of the auto-correlation function of the physical quantity. For example, the N-dimensional auto-correlation function of the physical quantity  $a$  can be written

$$\xi_N(\mathbf{l}) = \langle a(\mathbf{r})a(\mathbf{r} + \mathbf{l}) \rangle, \quad (1)$$

where  $\mathbf{r}$  is the spatial position and  $\mathbf{l}$  is the spatial separation. The N-dimensional power spectrum is then

$$p_N(k) = \int e^{i\mathbf{k} \cdot \mathbf{l}} \xi_N(\mathbf{l}) d\mathbf{l}, \quad (2)$$

where  $\mathbf{k} = (k_x, k_y, k_z)$  is the wavenumber, which is related to the scale by  $k = 2\pi/l$ , and the integration is performed over all N-dimensional space. The energy spectrum is the angle integral of the power spectrum over shells of radius  $k = |\mathbf{k}|$ , such that  $E_N(k) \propto k^{N-1} p_N(k)$ .

Often the power spectrum can be represented by a power law  $p_3(k) \propto k^n$ . For instance, the velocity field for incompressible, homogeneous (Kolmogorov 1941) turbulence has  $n = -11/3$ , while for shock-dominated turbulence (Burgers 1974), the 3D power-law index is  $n = -4$ .

### 2.3.2 Velocity centroid statistics

The use of positional fluctuations in the velocity centroids of spectral lines as probes of turbulent gas motions was developed in the 1950s by, for example, Münch (1958), and has been applied to observations of molecular emission lines in molecular cloud complexes (Dickman & Kleiner 1985; Kleiner & Dickman 1985) and to optical emission lines in the Orion Nebula, galactic and extragalactic H II regions (Roy & Joncas 1985; O'Dell & Castañeda 1987; Castañeda 1988; Lagrois et al. 2011).

The plane-of-the-sky velocity centroid map is calculated from the first two velocity moments  $M_j$  of the simulated line intensity maps  $I(v_r)$ , where

$$M_j = \int_{v_{s1}}^{v_{s2}} v_s^j I(v_s) dv_s, \quad (3)$$

and  $v_s$  is the radial (line-of-sight) velocity, for convenience taken to be along one of the principal axes of the 3D data cube. The centroids are then  $\mathbf{V}_c(x, y) = \mathbf{M}_1/M_0$ , where  $(x, y)$  is the projection plane (plane of the sky) when the line of sight is along the  $z$ -axis. The limits of the integration over velocity are  $v_{s1}$  and  $v_{s2}$ , which represent the full range of velocities produced by the simulations plus thermal broadening, where the thermal width is  $v_T = (kT/m_p)^{1/2}$  and  $m_p$  is the atomic mass.

The observed second-order structure function is

$$S_2(\mathbf{l}) = \frac{\sum [V_c(\mathbf{r}) - V_c(\mathbf{r} + \mathbf{l})]^2}{\sigma_c^2 N(\mathbf{l})}, \quad (4)$$

where the variance of centroid velocity fluctuations is

$$\sigma_c^2 \equiv \frac{\sum [V_c(\mathbf{r}) - \langle V_c \rangle]^2}{N}, \quad (5)$$

and  $\langle V_c \rangle$  is the mean centroid velocity

$$\langle V_c \rangle \equiv \frac{\sum V_c(\mathbf{r})}{N}. \quad (6)$$

In this definition,  $\mathbf{r}$  is the two-dimensional position vector in the plane of the sky and  $\mathbf{l}$  is the lag, or separation vector. The summation in Equation 4 is over all data pairs for each separation,  $N(\mathbf{l})$ , while the summations in the centroid variation and mean are over the total number of array elements, i.e., pixels in the  $(x, y)$ -plane.

For homogeneous, incompressible (Kolmogorov) turbulence, the velocity fluctuations scale as  $l^{1/3}$  and hence the second-order structure function scales like  $l^{2/3}$ . For isotropic velocity fields, the structure function and the auto-correlation function (see Eq. 1) have the same scaling and differ only by a constant. The structure function is therefore related to the power spectrum. If the power-law index of the

3D structure function is  $m$ , then the power-law index of the 3D power spectrum is  $n = -3 - m$ .

### 2.3.3 Velocity channel analysis

The relationship between the velocity centroids and the statistics of the velocity field is only reliable if the density fluctuations are negligible. Velocity channel analysis was developed to extract the separate contributions of density and velocity from spectral line data cubes.

This is a technique for analyzing position-position-velocity (PPV) cubes developed by Lazarian & Pogosyan (2000). With this method, spectroscopic observations are not reduced to velocity centroids as a function of position on the plane of the sky. Instead, the PPV cubes are analyzed in terms of velocity channels, or slices, as a function of the velocity resolution used. As the width of the velocity slices increases, the relative contribution of a velocity fluctuation to the total intensity fluctuations decreases, because the contributions from many velocity fluctuations will be averaged out in thicker velocity slices. A slice is described as *thick* when the dispersion of turbulent velocities is less than the velocity slice thickness on the turbulence scale studied, otherwise the slice is *thin* (Esquivel et al. 2003). In the thickest velocity channels, we obtain only information about the density fluctuations, since the velocity information is averaged out. Conversely, the velocity fluctuations dominate in thin channels.

Velocity channel analysis (VCA) consists of obtaining the 2D power spectrum for each velocity channel and then averaging over all velocity channels for each PPV cube. Esquivel et al. (2003) stress that whether a slice in velocity space is considered *thin* or *thick* depends not only on the slice width  $\delta v = (v_{\max} - v_{\min})/N$ , where  $N$  is the number of channels, but also on the scale of the turbulence. For power-law statistics, the velocity dispersion scales as  $\sigma_r \propto r^{m/2}$ , where  $m$  is the velocity structure function index. The criterion for a channel to be considered thin is  $\delta v < \sigma_r$ , hence we do not expect a pure power-law result from the averaged 2D power-spectra analysis. This is because the largest scales, of the order of the size of the cube, are almost always in the *thin* regime. At the smallest scales, numerical dissipation plays a rôle, and there is an additional deviation from the power law.

Taking into account the thermal width of the optically thin emission line introduces an additional limitation on the resolution that can be used to discriminate between the *thick* and *thin* regimes. For a fixed velocity resolution, a velocity channel will remain *thin* up to wavenumber

$$k \leq 2\pi \left[ \frac{1}{\sigma_L^2} (\delta v^2 + 2v_T^2) \right]^{-1/m}, \quad (7)$$

where  $\sigma_L$  is the velocity dispersion over the scale  $L$ , equivalent to the size of the computational domain, and  $v_T$  is the thermal width. The thermal width smears velocity fluctuations on smaller scales.

### 2.3.4 Projection Smoothing

The effect of projecting a three-dimensional correlation function onto a two-dimensional space has been studied by von

Hoerner (1951), Münch (1958), O'Dell & Castañeda (1987) and Brunt & Mac Low (2004), among others. For the velocity field, the two-dimensional case corresponds to the emission-line velocity centroid map.

Previous authors have established that for an isotropic, power-law, three-dimensional power spectrum, the spectral slope does not change on going from three dimensions to two (projected) dimensions, i.e.  $\kappa_{2D} = \kappa_{3D}$ , where  $\kappa_{ND}$  is the power spectrum spectral index in  $N$  dimensions (defined as  $p_N(k) \propto k^{-\kappa_{ND}}$ , Stutzki et al. 1998; Miville-Deschênes, Levrier, & Falgarone 2003; Brunt et al. 2003). This is because the line-of-sight contribution to the line-of-sight velocity has no amplitude on the  $k_z = 0$  plane, where  $z$  is the line-of-sight direction.

The relationship between the power spectrum spectral index and the exponent of the second-order structure function for homogeneous turbulence is  $\kappa_{ND} = m_{ND} + N$ , where  $m_{ND}$  is the slope of the  $N$ -dimensional second-order structure function. For projection from 3 to 2 dimensions, we therefore have  $m_{2D} = m_{3D} + 1$ , and this is known as *projection smoothing*.

In the case of incompressible, homogeneous (Kolmogorov) turbulence, we have  $\kappa_{3D} = 11/3$  and  $m_{3D} = 2/3$ , hence the relationship  $\kappa_{2D} = \kappa_{3D}$  leads to  $m_{2D} = 5/3$ . For the compressible turbulence (Burgers 1974) case, we have  $\kappa_{3D} = \kappa_{2D} = 4$  and  $m_{3D} = 1$ , leading to  $m_{2D} = 2$ . When the line-of sight depth is small compared to the plane-of-the sky size of the emitting region, the distribution of emitters is essentially two-dimensional (sheet-like) and we would expect  $m_{2D} \simeq m_{3D}$  (O'Dell & Castañeda 1987; Miville-Deschênes, Levrier, & Falgarone 2003).

In order to compensate for the effects of density inhomogeneities, Brunt & Mac Low (2004) introduced a correction term  $\delta\kappa$  such that  $\kappa_{2D} = \kappa_{3D} + \delta\kappa$ , where  $\delta\kappa$  tends to  $-1$  when density fluctuations are important. This idea was applied by Lacrois & Joncas (2011) in an effort to use 2D observational statistics to infer the 3D velocity field of photoionized gas in giant extragalactic H II regions.

## 3 RESULTS

### 3.1 General Properties

We begin by considering the morphological appearance of the simulated H II regions. Figure 1 shows the evolutionary sequence from 150,000 to 300,000 years. Each image is a composition of the three optical emission lines [N II]  $\lambda 6584$  (red), H  $\alpha$  (green) and [O III]  $\lambda 5007$  (blue), where we have employed the classical *Hubble Space Telescope* red-green-blue colour scheme. Emission from the dense, neutral zones is negligible and for the production of these images we also include dust extinction in the radiative transfer for the projection to the plane of the sky, with the assumption that the dust-to-gas mass ratio is 1%.

The images show that the ionized gas distribution is not spherical and around the corrugated edge of the H II region there are many neutral clumps and fingers of gas. This is a consequence of the H II region evolving in a clumpy neutral medium. The fingers and clumps at the edge of the H II region are the remnants of denser regions in the initial turbulent cloud. We can also see that the different ions



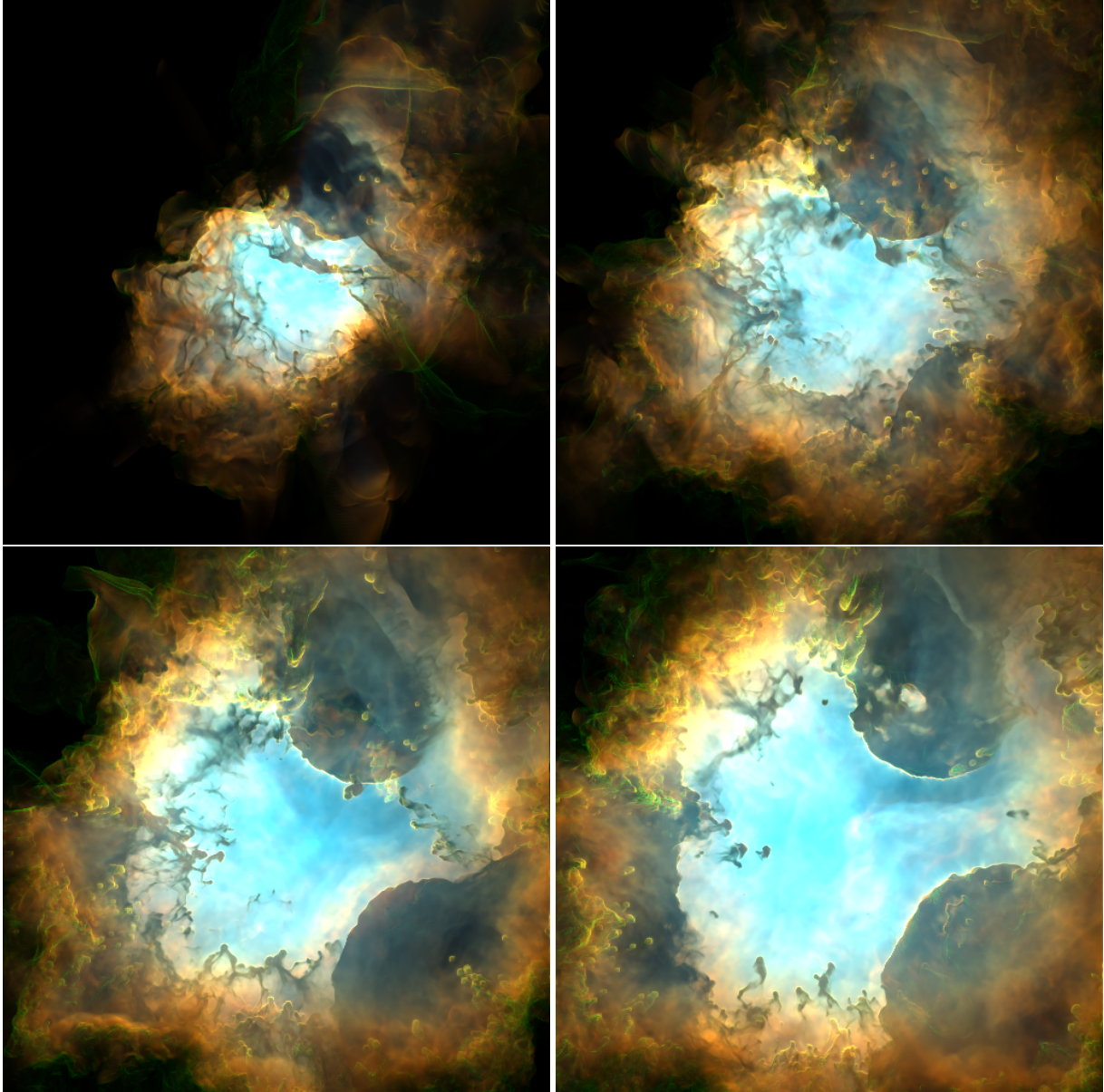


**Figure 1.** Simulated projected emission-line images of an evolving H II region in a turbulent molecular cloud. The panels show the H II region at 150,000, 200,000, 250,000 and 300,000 yrs, from top left to bottom right. The physical size of each image is 4 pc on a side and the resolution of the simulation is  $512^3$  cells. The view is from the negative- $z$  direction of the computational cube. The colours represent the optical emission lines [N II] $\lambda$ 6584 (red), H $\alpha$  (green), and [O III] $\lambda$ 5007 (blue), and for these images the effect of dust absorption has been included in the radiative transfer during the projection onto the plane of the sky.

are important in different regions of the photoionized gas. The [O III] $\lambda$ 5007 (blue) emission is strongest closer to the photoionizing source, while the [N II] $\lambda$ 6584 (red) emission is most prominent around the edge of the H II region and the H $\alpha$  is distributed throughout the nebula. Although not shown in Figure 1, we also calculate the [S II] $\lambda$ 6716 emission, which is important only around the edge of the H II region in the vicinity of the ionization front. This is consistent with the phenomenon of ionization stratification (Osterbrock & Ferland 2006).

The neutral clumps and fingers around the edge of the H II region are the source of photoevaporated flows, which flow away from the ionization front into the H II region (Hen-

ney 2003). These flows are mildly supersonic and can reach velocities of up to two or three times the sound speed in the ionized gas. They shock against each other in the interior of the H II region. Neutral clumps inside the H II region are accelerated outwards by the rocket effect in the opposite direction to the photoevaporated material flowing off their ionized skins. In Figure 1 these photoevaporated flows can be discerned as shadowy regions ahead of the convex bright cusps that mark the position of the ionization front. As the photoevaporated gas flows away from the ionization front, the density drops in the diverging flow and this is why the flows appear darker than the surrounding photoionized gas.

These colliding photoevaporated flows are responsible

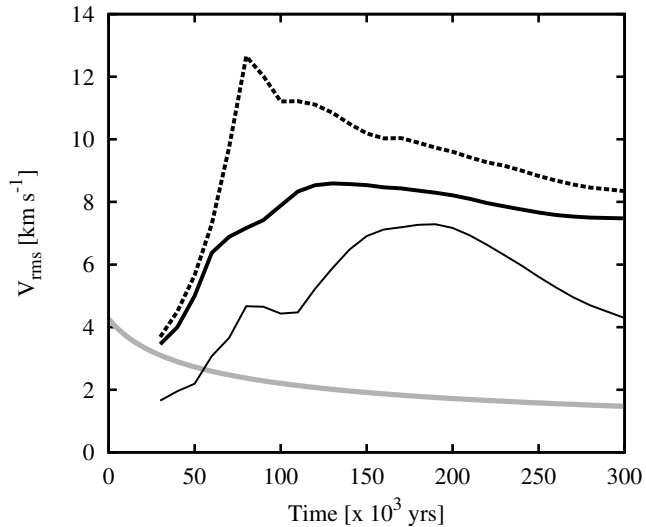


**Figure 2.** Velocity dispersion as a function of time. The **thick, black solid line** shows the **mass-weighted** velocity dispersion of the ionized gas, the dotted line is the **volume-weighted** velocity dispersion of the ionized gas, while the thick grey line is the r.m.s. velocity of the analytical expansion (Spitzer 1978) in a uniform medium of density  $n_0$ . The **thin, black continuous line** is the **mass-weighted mean radial expansion velocity** of the ionized gas.

for the velocity dispersion of the ionized gas, which we show in Figure 2. This figure shows both the **mass-weighted velocity dispersion of the ionized gas** and the **volume-weighted velocity dispersion**. At early times ( $t < 10^5$  yrs) the volume-weighted velocity dispersion is higher than that of the mass-weighted velocity dispersion. This is because the H II region breaks out of the dense clump where it is formed after about 50,000 yrs and a low-density, relatively high velocity champagne flow results. After about 100,000 yrs, the main ionization front has just about caught up and thereafter the two different velocity dispersions show the same behaviour, remaining roughly constant with  $V_{\text{rms}} \sim 8 \text{ km s}^{-1}$ . In Figure 2 we also show the r.m.s. velocity for the analytical expansion (Spitzer 1978) in a uniform medium, where the gas velocity behind the ionization front is one half that of the ionization front and the internal velocities are linear with radius. In this case, the velocity dispersion falls steadily as a function of time, and after 100,000 yrs is less than  $2 \text{ km s}^{-1}$ . The differences between the velocity dispersions in the numerical and analytic cases are entirely due to the interaction of the photoevaporated flows produced in the simulations described above. In the analytic expansion, the velocities are radial away from the central source. In the clumpy medium, the photoevaporated flows lead to large non-radial velocities, which increase the velocity dispersion in the photoionized region. Finally, Figure 2 also shows that the **mass-weighted mean radial velocity** peaks just before 200,000 yrs at about  $7 \text{ km s}^{-1}$  and thereafter falls off. This indicates that the global expansion will not be an important influence on the dynamics, compared to the velocity dispersion, after 200,000 yrs.

## 3.2 Statistical Properties

### 3.2.1 Power Spectra

In Figure 3 we show the 3D power spectra of the ionized gas velocity, the ionized density, and the ionized velocity weighted by the cube root of the density (see, e.g., Kritsuk et al. 2007). **In the following sections we use a dimensionless  $k$  that is normalised to the size of our computational grid. Thus  $k = 1$  corresponds to a physical scale of 4 pc.** The power spectra all exhibit a break in the power law at about wavenumber  $k \sim 32$ , equivalent to a scale of 16 computational cells and consistent with the numerical dissipation scale. We fit power laws between  $k = 4$  (corresponding to a length scale of one parsec) and  $k = 32$ . For times later than 200,000 yrs, the power-law fits for a given quantity are essentially constant (see Fig. 4). Note that here we use  $n$  to represent the 3D power spectrum spectral index,<sup>1</sup> where  $n = -\kappa_{3D}$  and  $\kappa_{3D}$  is defined in § 2.3.4. At earlier times, the power laws are steeper and evolving. This behaviour mimics, with a delay of about 50,000 yrs, the velocity dispersion behaviour seen in Figure 2. **The flattening-off of the power spectra corresponds to the time at which the global expansion ceases to be important for the internal dynamics (see Fig. 2).**

In Figure 5 we compare the sound-crossing time of the ionized volume with the evolution time of the simulation. During the breakout of the H II region from its initial dense clump (between about 80,000 and 100,000 yrs), the expansion is supersonic and the sound-crossing time exceeds the evolution time. This coincides with the peak in the velocity dispersion (see Fig. 2). After this time, the expansion is subsonic and the sound-crossing time becomes shorter than the evolution time. A statistically steady state then becomes possible for the turbulence within the ionized volume. This occurs after about 200,000 yrs (as evidenced in Fig. 4), which corresponds to the evolution time being equal to approximately 1.5 times the sound-crossing time.

### 3.2.2 Second-order Structure Functions

We use the procedure described in Section 2.3.2 to calculate velocity centroid maps for the H $\alpha$ , [O III] $\lambda 5007$ , [N II] $\lambda 6584$  and also [S II] $\lambda 6716$  emission lines and then calculate the corresponding second-order structure functions according to Equation 4. **Results for representative evolutionary times are shown in Figures A1 to A3 of Appendix A, where power law fits to the slope ( $m_{2D}$ ) of the structure function are carried out for the inertial range of scales.**

In Figure 6 we show the evolution of  $m_{2D}$  with time for the different lines and for the three principal viewing directions of the simulation cube. For the line of sight along the  $z$ -axis (first column of Fig. 6), one sees for all lines a consistent steepening of the structure function graph with time (increase in  $m_{2D}$ ). But for other viewing directions no such trend is apparent: both rising and falling behavior of  $m_{2D}$  is seen, with little consistency between different lines.

In order to understand why one particular viewing direction is different, we produced histograms of the emission-

<sup>1</sup> This is to facilitate comparison with the theoretical literature, such as Lazarian & Pogosyan (2000) .

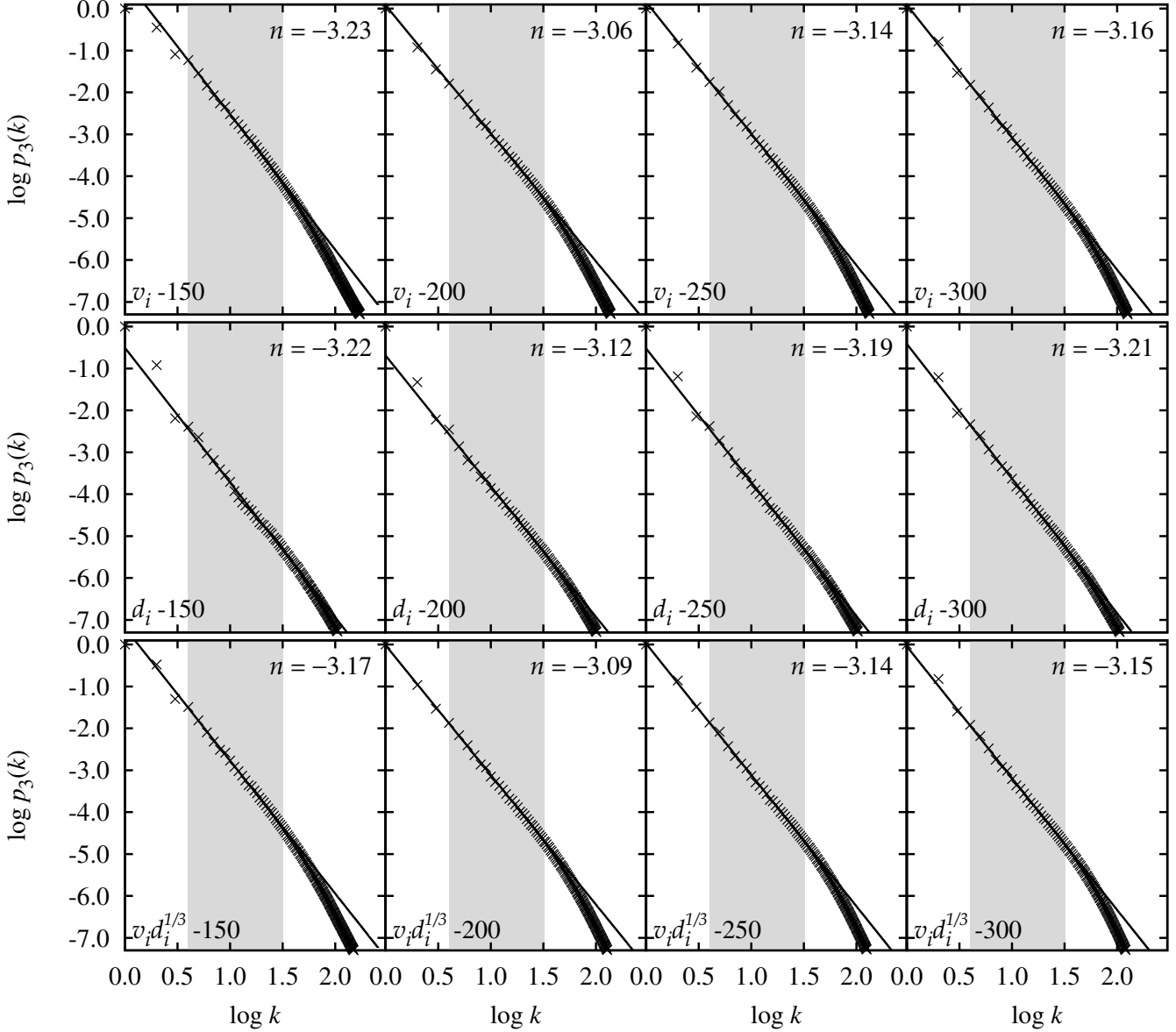


**Figure 3.** Power spectra of the 3D simulation cube. From top to bottom: ionized gas velocity  $v_i$ , ionized gas density  $d_i$ , ionized gas velocity weighted by the cube root of the density  $v_i d_i^{1/3}$ . From left to right: 150,000, 200,000, 250,000 and 300,000 years. The points represent the calculated power spectra for the numerical simulation and the solid line is the least-squares fit to the data points between limits described in the text, represented by the grey rectangle.

line velocity centroid values binned into narrow  $< 2 \text{ km s}^{-1}$  bins for the three different lines of sight at the four different times. The histograms are presented in Figure 7, from which we see that for the  $z$ -axis line of sight, the values of  $V_c$  are not distributed symmetrically about the mean value and, in fact, for the  $\text{H}\alpha$  and  $[\text{O III}]\lambda 5007$  emission lines, a “wing” develops for negative values of  $V_c$  that extends to more negative values as time progresses. This tendency is not seen for the  $y$ - and  $x$ - axis lines of sight. We attribute this wing to a “champagne” flow towards the observer along the  $z$ -axis. This flow would be perpendicular to the line of sight for observations along the other axes.

### 3.2.3 Velocity Channel Analysis

Figure 8 shows the evolution with time of the VCA slope from thin and thick channels (shown by filled circle and cross symbols, respectively) for different ions and for different viewing directions. The individual VCA power spectra from which these slopes were extracted are presented in Appendix B. It can be seen that both  $\gamma_t$  and  $\gamma_T$  are remarkably stable with time during the latter part of the evolution ( $t > 200,000$  years). Although thermal broadening means that there is no clear distinction between  $\gamma_t$  and  $\gamma_T$  for the  $\text{H}\alpha$  line, the two values are clearly distinguished for the heavier ions, with the thin slices showing a significantly shallower slope, especially for  $[\text{O III}]$ . The implications for diagnosing turbulence statistics are discussed in § 4.1.3.

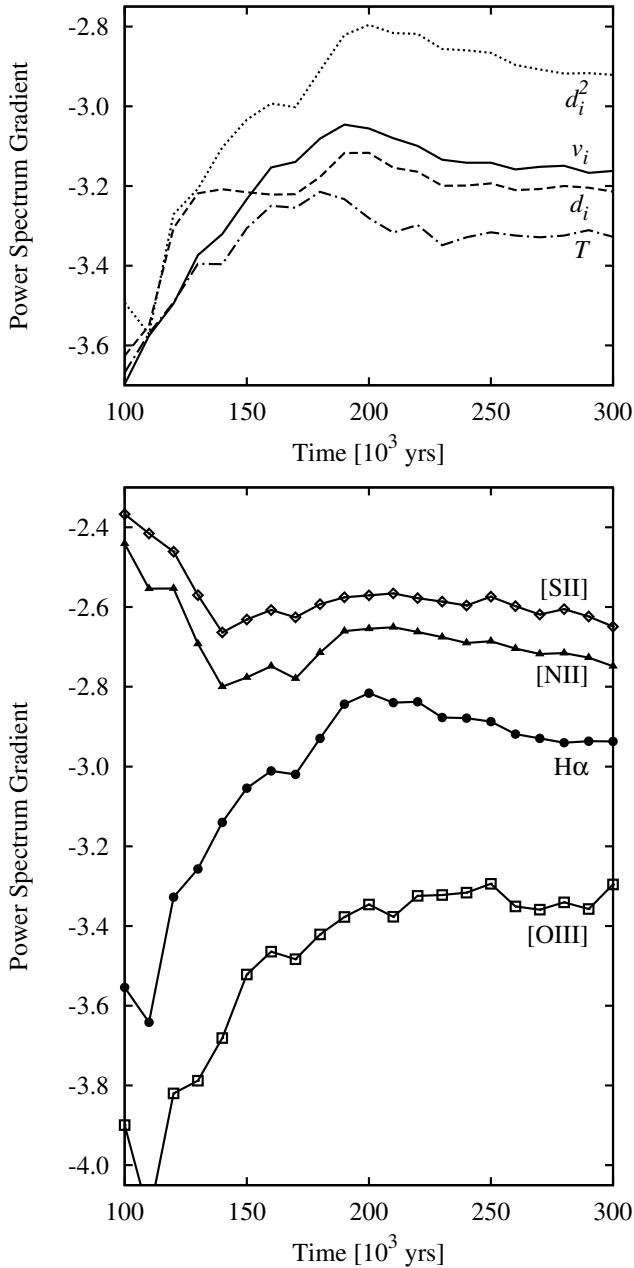


**Figure 4.** Time variation of 3D power-spectra gradients. Top panel: 3D physical quantities. Solid line—ionized gas velocity  $v_i$ , dashed line—ionized density  $d_i$ , dotted line—square of ionized density  $d_i^2$ , dot-dashed line—temperature  $T$ . Bottom panel: emission-line volume emissivities. Filled circles— $j(\text{H}\alpha)$ , open squares— $j([\text{OIII}])$ , filled triangles— $j([\text{NII}])$ , open diamonds— $j([\text{SII}])$ .

## 4 DISCUSSION

### 4.1 Characterization of the turbulence from optical emission lines

At times later than 150,000 years, our second-order structure function results for the  $\text{H}\alpha$  and  $[\text{OIII}]\lambda 5007$  emission-line velocity centroids strongly suggest the presence of turbulence with an inertial range between 1 pc and the numerical dissipation scale of about 8 cells (equivalent to 0.0625 pc). The

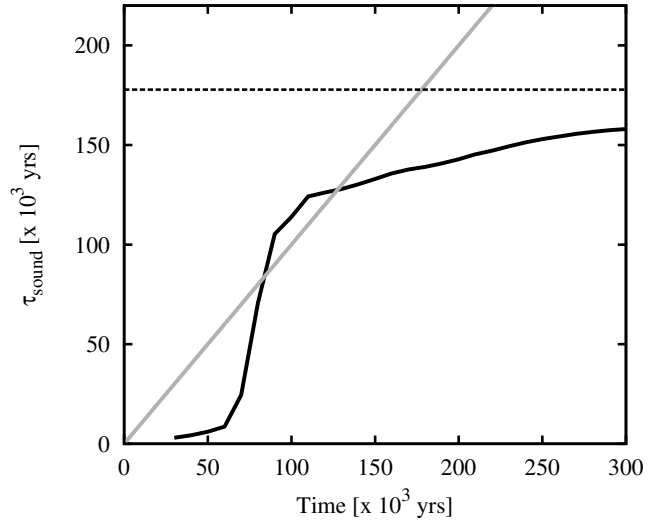


**Figure 5.** Sound crossing time as a function of evolution time. The sound crossing time is  $\langle R \rangle / c_i$ , where  $\langle R \rangle$  is the radius of an equivalent sphere with volume equal to that of the  $\text{H II}$  region and  $c_i = 11 \text{ km s}^{-1}$  is the sound speed in the photoionized gas. The diagonal grey line has slope of unity. The horizontal dashed line is the sound crossing time for a distance of 2 pc, which is the half-side length of the computational box.

$[\text{NII}]\lambda 6584$  and  $[\text{SII}]\lambda 6716$  structure function results also suggest turbulence, with a smaller upper limit to the inertial range, which is consistent with these ions being confined to relatively thin layers near the ionization front. However, it is difficult to characterize this turbulence since the slope of the structure function for a given emission line varies with time in a non-predictive manner and also depends on the line of sight. Although the results for the  $z$ -axis line of sight suggest an increase in slope with time, an examination of the distributions of the velocity centroids (see Fig. 7) showed that this is due to a champagne-type flow in that direction, and other lines of sight do not show a definite trend with time.

Different emission lines originate in different volumes of ionized gas, and this is reflected in the different slopes for the structure functions from different emitters. The  $\text{H}\alpha$  line is produced throughout the volume and is brightest close to the ionization front around the bright edges of the photoionized gas. There is therefore a wide range of densities associated with the  $\text{H}\alpha$ -emitting gas. The emissivity of the  $\text{H}\alpha$  recombination line depends on the square of the density and only weakly on the temperature in the photoionized gas (see e.g., Osterbrock & Ferland 2006). Indeed, the gradients of the 3D power spectra of the  $\text{H}\alpha$  emissivity and the square of the density are essentially the same. On the other hand, the  $[\text{OIII}]\lambda 5007$  emission comes from the inner region of the  $\text{H II}$  region, where the density is more uniform. However, the emissivity of this collisional line is a more complicated function of temperature, and the  $\text{O}^{++}$  ion is found in the more central regions of the  $\text{H II}$  region, where shocks due to photoevaporated flows cause fluctuations in the temperature. A more uniform density distribution corresponds to a steeper density power spectrum and, indeed, the structure functions, 2D velocity channel power spectra, and 3D power spectrum



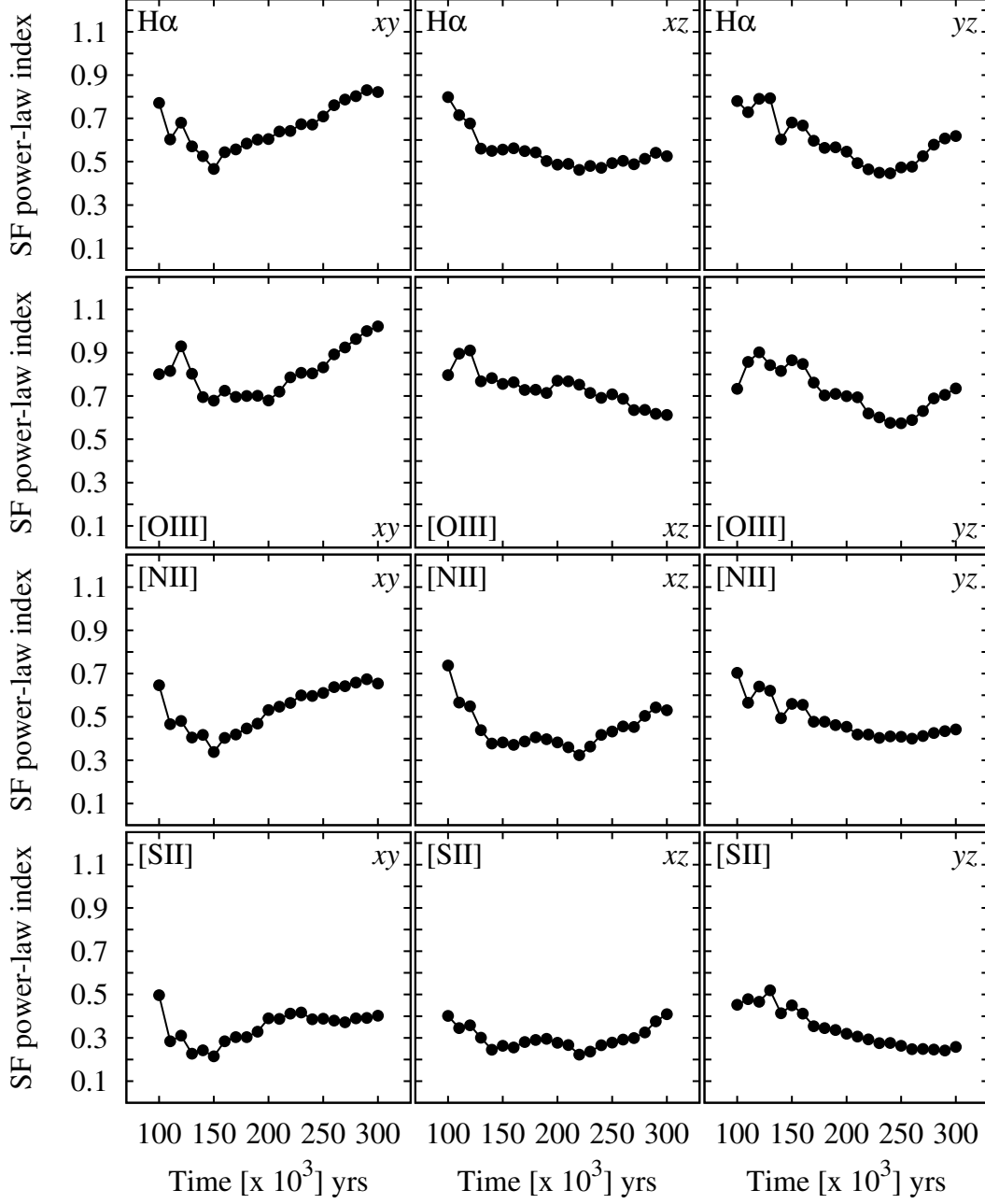


**Figure 6.** Evolution of second-order structure function power-law index,  $m_{2D}$ , as a function of time. From top to bottom:  $H\alpha$ ,  $[OIII] \lambda 5007$ ,  $[NII] \lambda 6584$ ,  $[SII] \lambda 6716$ . From left to right: line of sight along the  $z$ ,  $x$  and  $y$  axes, respectively.

of the  $[OIII] \lambda 5007$  line are all steeper than those for the  $H\alpha$  recombination line.

The stellar parameters for the simulations presented in this work correspond to a relatively hot (37,500 K) O7 star. For these parameters, the  $[NII] \lambda 6584$  and  $[SII] \lambda 6716$  collisionally ionized lines come from regions close to the ionization front, where the density variations are strong, and this is reflected in the less steep structure function and 2D velocity channel power spectra gradients. In particular, the  $[SII]$  emission will come from very close to the ionization front where the acceleration of the ionized gas is strongest, and as a result the structure function and 2D velocity channel power-spectra gradients are shallowest for this line. Other

stellar parameters, e.g., a cooler B0 star or a much hotter white dwarf, would produce photoionized regions with different ionization stratifications.

#### 4.1.1 Intrinsic Power Spectra Of Physical Quantities

Figure 3 shows that the power spectra of physical quantities are very well approximated by power laws over the range from  $k = 4$  to 32 (scales of 1 pc to 0.125 pc). In particular, the ionized gas velocity shows a power-law slope of  $n = -3.2 \pm 0.1$  once the turbulence is fully developed. This is significantly shallower than the Kolmogorov ( $n = -3.667$ ) or Burgers ( $n = -4$ ) value, indicating more velocity struc-

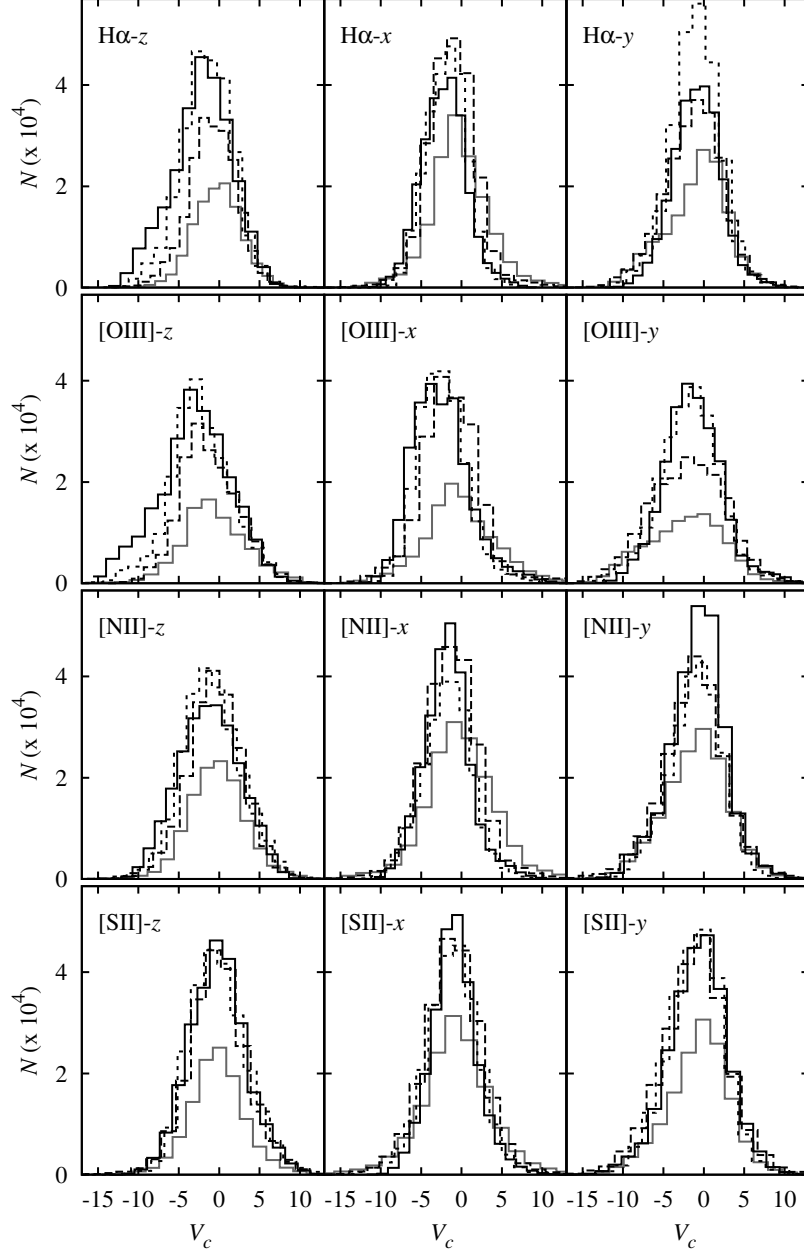


**Figure 7.** Histograms of velocity centroid values for each emission line along different lines of sight. From top to bottom:  $H\alpha$ ,  $[O\text{ III}]\lambda 5007$ ,  $[N\text{ II}]\lambda 6584$ ,  $[S\text{ II}]\lambda 6716$ . From left to right: line of sight along the  $z$ ,  $x$  and  $y$  axes, respectively. The different line types refer to different times: thick, grey line—150,000 yrs, dashed line—200,000 yrs, short-dashed line—250,000 yrs, continuous black line—300,000 yrs.

ture at small scales than would be seen in a simple turbulent cascade of energy injected at the largest scale. As a consequence, the turbulent velocity dispersion is relatively insensitive to scale, varying as  $\sigma \sim l^{0.5(-3-n)} \sim l^{0.1}$ .

One possible reason for the shallow velocity power spectrum may be that energy is injected over a variety of scales, corresponding to the different sizes of clumps and filaments responsible for the photoevaporated flows in the simulated  $H\text{ II}$  regions. Moreover, the energy injection will vary with time due to the global expansion of the  $H\text{ II}$  region, which moves the sources of the photoevaporated flows generally outwards, and the destruction of the clumps and filaments as they are eroded by the ionizing radiation.

The density power spectrum has a very similar slope to that of the velocity:  $n = -3.2 \pm 0.1$ , but of greater relevance are the slopes of the emissivities of the different emission lines, which are  $n = -3.4 \pm 0.1$  for  $[O\text{ III}]$ ,  $n = -2.9 \pm 0.1$  for  $H\alpha$ ,  $n = -2.7 \pm 0.1$  for  $[N\text{ II}]$ , and  $n = -2.6 \pm 0.1$  for  $[S\text{ II}]$ . These span the critical value of  $n = -3$  that divides “steep” from “shallow” power spectra.  $[O\text{ III}]$  has a steep slope, indicating that large-scale fluctuations dominate, while  $[N\text{ II}]$  and  $[S\text{ II}]$  have shallow slopes, indicating that small-scale fluctuations dominate. The  $H\alpha$  slope is very close to the critical value, indicating roughly equal contributions from fluctuations on all size-scales.

It is interesting to study the question of whether the

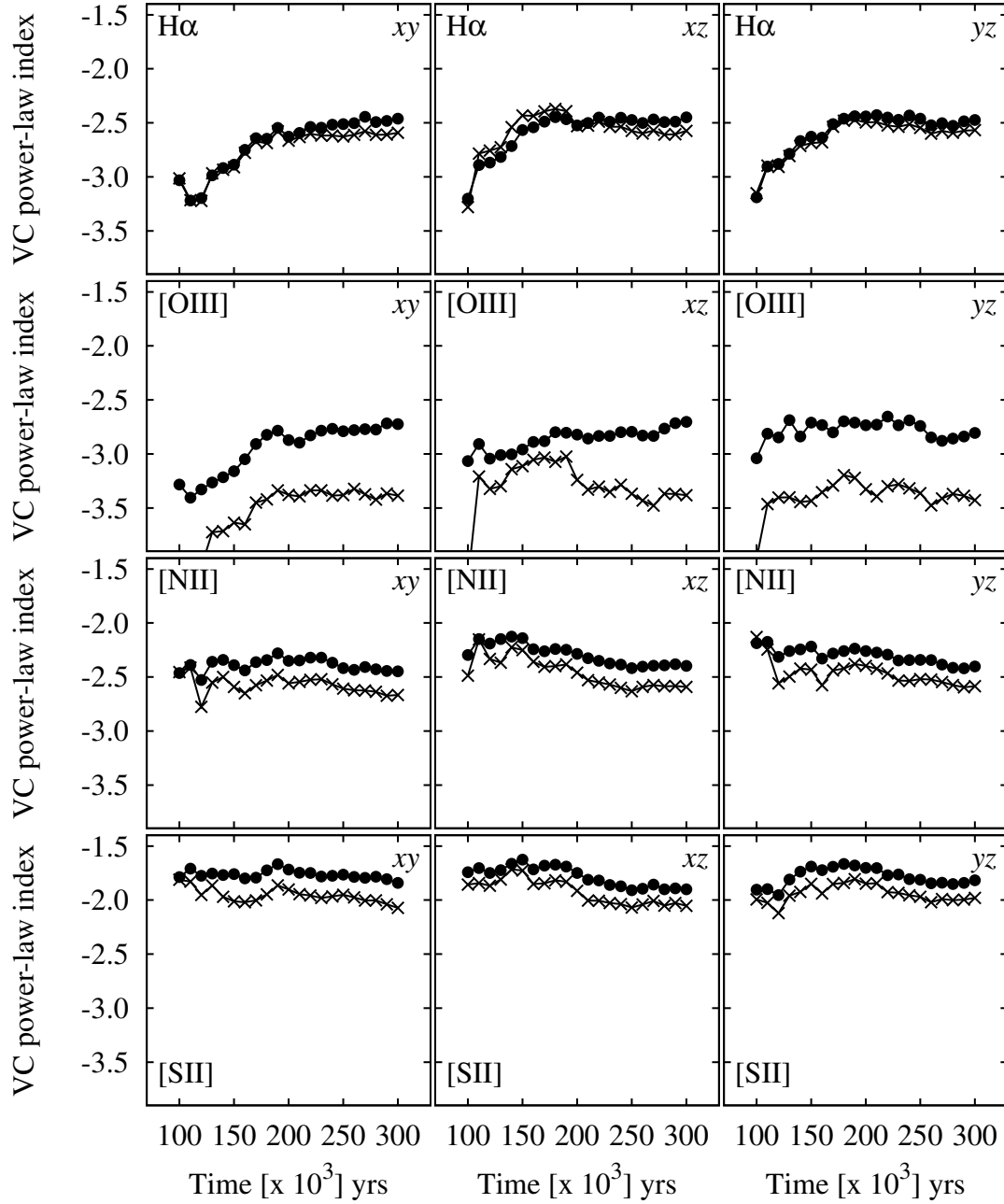


**Figure 8.** Evolution of velocity channel power-law index as a function of time for thick channels ( $\gamma_T$ ; crosses) and thin channels ( $\gamma_t$ ; filled circles). From top to bottom:  $H\alpha$ ,  $[O\text{ III}] \lambda 5007$ ,  $[N\text{ II}] \lambda 6584$ ,  $[S\text{ II}] \lambda 6716$ . From left to right: line of sight along the  $z$ ,  $x$  and  $y$  axes, respectively. Thermal broadening was included in all cases.

known power-law indices of the velocity and emissivity power spectra in our simulations can in practice be recovered from observational diagnostics. If this is not the case for a given diagnostic, then it would call into question its utility for studying real HII regions. In particular, we will concentrate on two commonly used diagnostics: the second-order structure function of the line velocity centroids, and the power spectra of the surface brightness in isovelocity channel maps (Velocity Channel Analysis).

#### 4.1.2 Structure Function

The structure function of the velocity centroids is an observationally attractive diagnostic because it is relatively immune to the effects of thermal broadening and poor spectral resolution, so long as sufficiently high signal-to-noise spectra are used. However, it has the disadvantage that relating the observed slope to the 3-dimensional velocity statistics depends on the geometry of the emitting region, see § 2.3.4. For transverse separations larger than the characteristic line-of-sight depth of the emitting gas, the two-dimensional gradient should be equal to the three-dimensional one:

$$m_{2D} = m_{3D} = -3 - n,$$

whereas at smaller separations than this, projection smoothing, as described above, means that the two-dimensional gradient is steeper:

$$m_{2D} = 1 + m_{3D} = -2 - n.$$

Based on our simulation’s velocity power spectrum index at late times of  $n \approx -3.2$  (see Figs. 3 and 4), the structure function slope should be  $m_{2D} = 0.2$  in the large-scale limit and  $m_{2D} = 1.2$  in the small-scale limit.

In fact, all of the measured slopes lie between these two limits, with a systematically increasing value from low to high-ionization lines:  $m_{2D}([S II]) = 0.33 \pm 0.02$ ,  $m_{2D}([N II]) = 0.49 \pm 0.03$ ,  $m_{2D}(H\alpha) = 0.59 \pm 0.04$ ,  $m_{2D}([O III]) = 0.74 \pm 0.04$ , where the averages were performed for  $t > 200,000$  years. This is qualitatively consistent with expectations because the emission from lower-ionization lines is confined to thin layers near the ionization front, whereas higher ionization emission is more distributed over the volume and therefore subject to greater projection smoothing.

If the line-of-sight depth were constant over the face of the H II region, then the structure function would show a break at a scale equal to that depth, but in reality the depth varies from point to point, so there will not be a sharp break. Instead, the structure function is expected to show negative curvature, with the gradient gradually decreasing as one passes from smaller to larger scales. A small such effect is seen in the structure functions derived from our simulations (Fig. A1 to A3): the fit to a power law is generally not so good as in the case of the power spectra, with negative residuals at both ends of the fitted range, indicative of a negative curvature. That the observed effect is so small is probably due to the fact that the distribution of line-of-sight depths strongly overlaps with the limited dynamic range in separations available from our simulations, bounded at small scales by numerical dissipation, and at large scales by the size of the ionized region.

It is disappointing that none of the measured slopes reach either of the limiting cases discussed above. All that can be deduced from the structure function is that  $1 + m_{3D} > m_{2D}([O III])$  and  $m_{3D} < m_{2D}([S II])$ , which implies  $n = -2.74$  to  $-3.33$ . Although this is a rather wide range of allowed velocity power spectrum slopes, it does serve to clearly rule out the Kolmogorov value of  $n = -3.667$ . Furthermore, the “true” value of  $n = -3.12 \pm 0.03$  lies close to the middle of the allowed range.

A further proviso to the use of the structure function is that systematic anisotropic flows can affect the measured slopes when the viewing angle is along the direction of the flow. Such an effect is seen at later times for our simulation when viewed along the  $z$ -axis (Fig. A1). In this case, the structure function tends to steepen at the large-scale end of our fitting range, producing a positive curvature, which is opposite to the more typical case of negative curvature discussed above. Such cases may also be identified by the presence of a significant skew in the PDF of the line-of-sight velocity (see Fig. 7).

Figure 9 illustrates these points by graphing the correlation between the structure function slope  $m_{2D}$  and the slope  $n$  of the underlying 3D velocity fluctuations. The theoretical relation is shown by black diagonal lines, both with (contin-

uous line) and without (dashed line) projection smoothing. It is apparent that a large part of the variation in  $m_{2D}$  is not driven by changes in  $n$ . Indeed,  $m_{2D}$  shows a larger or equal variation in the latter stages of evolution, when  $n$  is approximately constant, than it does in the earlier stages, when  $n$  is varying.

Note that the additional complication identified by Brunt & Mac Low (2004), whereby correlations between density and velocity fluctuations affect the translation between  $m_{2D}$  and  $n$ , is likely of minor importance in our case. Esquivel et al. (2007) show that this is most important for high Mach number turbulence, where  $\delta\rho/\langle\rho\rangle > 1$ , whereas the transonic turbulence inside our simulated H II regions produces more modest density contrasts.

#### 4.1.3 Velocity Channel Analysis

The velocity channel analysis consists of calculating the two-dimensional power spectrum of the brightness distribution in isovelocity channels of varying thickness. We consider two cases: thick slices, which are wide enough ( $\sim 100 \text{ km s}^{-1}$ ) to include all the emission in the line, and thin slices, with width  $5 \text{ km s}^{-1}$ . Because the velocity spectrum in our simulations is rather shallow (see above), the line-of-sight turbulent velocity dispersion  $\delta v$  exceeds the width of these thin slices over the full range of length scales that we can usefully study, from  $0.1 \text{ pc}$  ( $\delta v \approx 8 \text{ km s}^{-1}$ ) to  $1 \text{ pc}$  ( $\delta v \approx 10 \text{ km s}^{-1}$ ). Figure 10 shows typical examples of the [O III] brightness in thick and thin slices.

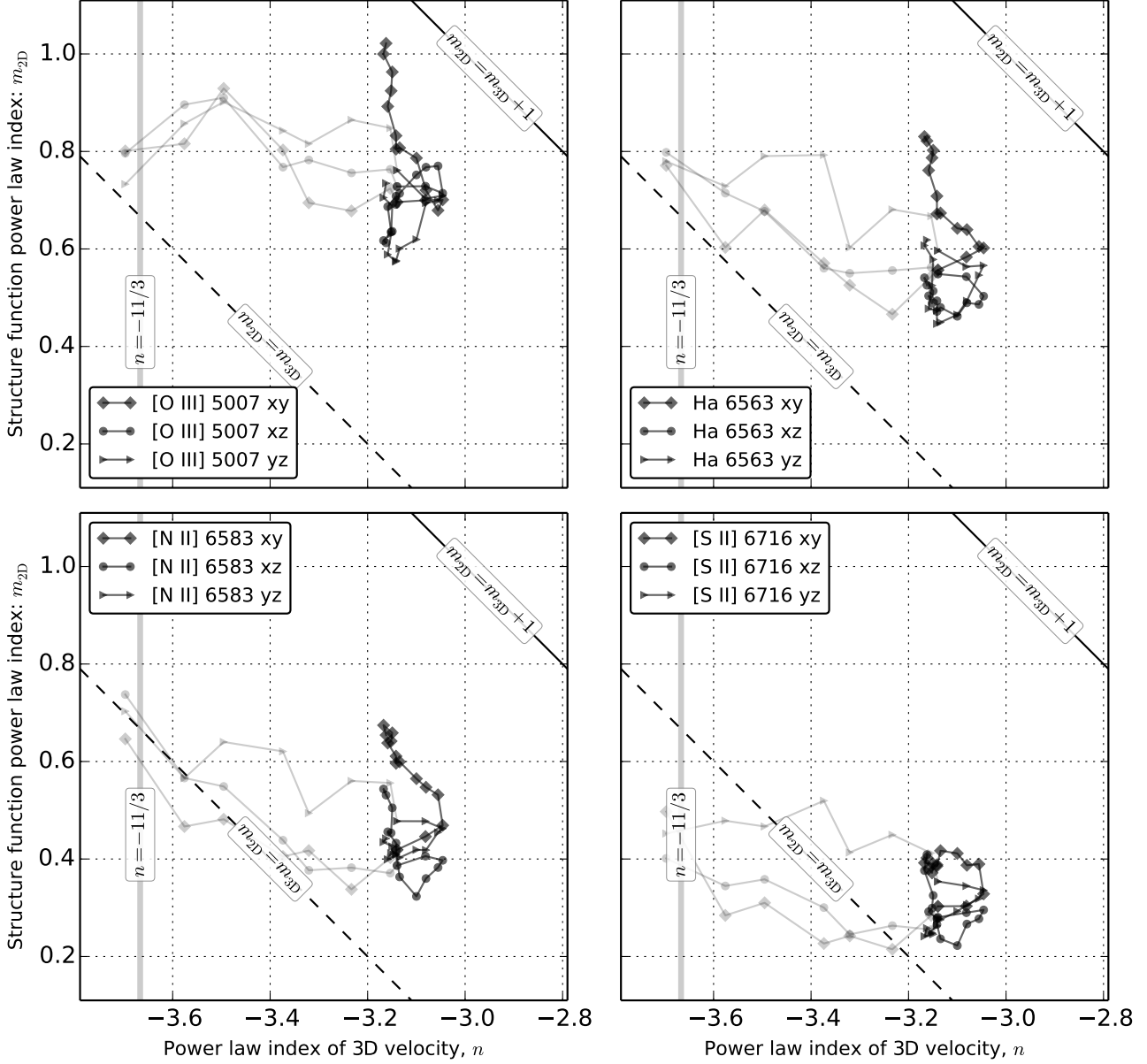
To use thinner slices would not be useful for a variety of reasons. First,  $5 \text{ km s}^{-1}$  corresponds to the highest resolution that can be achieved with optical spectrographs that are optimised for studying extended sources, such as Keck HIRES or VLT UVES. Second, thinner slices are increasingly subject to “shot noise” due to the finite resolution of the numerical simulations, which produces spurious small-scale power, as discussed by Esquivel et al. (2003) and Miville-Deschênes, Levrier, & Falgarone (2003). Third, thermal broadening would smoothe out any structure on scales  $< 5 \text{ km s}^{-1}$  for all but the heaviest ions.

Figure 11 shows the correlations between the slope of the velocity fluctuation power spectrum and the VCA slopes found in § 3.2.3 above (see Fig. 8). The theoretical procedure (Lazarian & Pogosyan 2000) for deriving one from the other is slightly different, depending on whether the power spectrum of the emissivity fluctuations is “steep” or “shallow” (see § 2.3.3 above). In the steep case, which applies to [O III] in our simulation, the slope of the average power spectrum of the brightness maps in the thin isovelocity channels is given by  $\gamma_{\text{thin}} = -3 + \frac{1}{2}m_{3D}$ , where  $m_{3D} = -3 - n = 0.2 \pm 0.1$  for our simulation. The derived value from the [O III] thin channel maps for  $t > 200,000$  is  $\gamma_{\text{thin}} = -2.80 \pm 0.07$ , which compares well with the value  $-2.9 \pm 0.05$  that is implied by the simulation’s value of  $n$ .

In the shallow case, it is the difference in slope between the thin and thick slices that is predicted to depend on the velocity fluctuations:  $\gamma_{\text{thin}} - \gamma_{\text{thick}} = \frac{1}{2}m_{3D}$ . The derived values are  $\gamma_{\text{thin}} - \gamma_{\text{thick}} = 0.07 \pm 0.05$ ,  $0.19 \pm 0.02$ , and  $0.17 \pm 0.02$  for H $\alpha$ , [N II], and [S II], respectively. These also compare tolerably well with the value of  $0.1 \pm 0.05$  that is implied by the simulation’s value of  $n$ .

Note, however, that the large Doppler width of the H $\alpha$





**Figure 9.** Structure function slope versus velocity power law slope. Each panel shows a different emission line; clockwise from upper left: [O III], H $\alpha$ , [S II], [N II]. Structure function slopes are shown for the 3 principal viewing directions, distinguished by different symbol types (see key). Dim gray lines and symbols show evolutionary times  $< 200,000$  years, while black lines and symbols show times  $> 200,000$  years.

line means that the thin velocity slices are not useful in this case, since the thick and thin slices have identical slopes. The fact that this agrees with the theoretical prediction is merely a coincidence, due to our velocity spectrum having a slope that is close to  $-3$ . For the lines from heavier ions, [O III], [N II] and [S II], the difference between the thin and thick velocity slices is not erased by thermal broadening, but in these three cases there is a consistent difference of  $\approx 0.1$  between the measured VCA slope and the theoretically expected one. The origin of this difference is unclear, but it is small enough that it is not a significant impediment to the application of the VCA method.

The slopes of the power spectra of the thick slices themselves, which are simply the velocity-integrated surface brightness images<sup>2</sup> are predicted (Lazarian & Pogosyan 2000) to be equal to the slopes of the 3D power spectra of their respective emissivities. The comparison between these two quantities is shown in Figure 12, from which it is clear that only in the case of [O III] are the two slopes equal. In the case of the other lines,  $\gamma_{vthick}$  is shallower than the emissivity's spectral index  $n$  by 0.36, 0.19, 0.61 for H $\alpha$ , [N II], and [S II], respectively. The reason for this dis-

<sup>2</sup> Although for simplicity, extinction is not included.

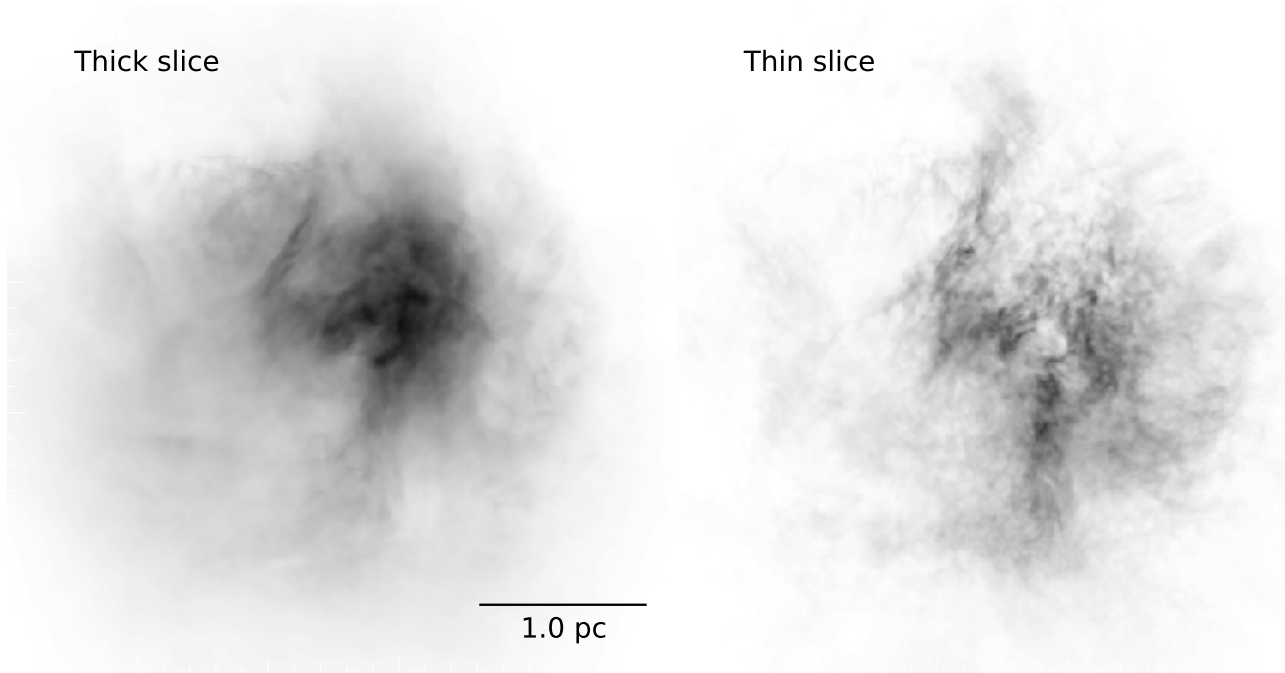


**Figure 10.** Surface brightness maps in thick (left) versus thin (right) velocity slices for the [O III] line from our simulation at an age of 300,000 years. The thick slice covers the full velocity range of the emission line, while the thin slice has a width of  $5 \text{ km s}^{-1}$ , which is smaller than the turbulent velocity fluctuations, but slightly larger than the thermal broadening for this line. It is apparent that the thin slice shows considerably greater small-scale structure than the thick slice, which is reflected in its shallower power spectrum. The brightness structure in the thick slice is due entirely to the emissivity fluctuations within the H II region, whereas the additional structure in the thin slice is caused by velocity fluctuations.

crepancy is the increasingly “sheet-like” morphology of the emission in the lower ionization lines. As shown in § 4.1 of Miville-Deschênes, Levrier, & Falgarone (2003), one should see a transition from  $\gamma_{\text{vthick}} = n$  to the shallower slope  $\gamma_{\text{vthick}} = n + 1$  at transverse scales larger than the line-of-sight depth of the emitting region.

#### 4.2 Comparison with observational results

Non-thermal linewidths in H II regions have been interpreted as evidence for turbulence in the photoionized gas. Galactic H II regions generally exhibit subsonic turbulent widths (Roy & Joncas 1985; O’Dell 1986), while giant extragalactic H II regions can have supersonic turbulent motions (Beckman & Relaño 2004; Lagrois et al. 2011). The majority of observational studies consider only the H $\alpha$  line, but O’Dell & Townsley (1988) and Castañeda (1988) examine the components of the [O III] $\lambda 5007$  line in the Orion Nebula, M42, while O’Dell & Wen (1992) and Wen & O’Dell (1993) investigate the kinematics of the [S III] and [OI] lines of this same object. The giant extragalactic H II region NGC-595 was studied by Lagrois & Joncas (2011) who analyzed the H $\alpha$ , [O III] and [S II] kinematics. The heavier ions have the advantage that their emission lines have low thermal broadening compared to the H $\alpha$  line.

Observational studies of the spatial scales of velocity fluctuations have mostly focused on the structure function of velocity centroids. The results are rather disparate, partly because the methodology varies considerably between different studies. For instance, some authors attempt to filter out “ordered” large-scale motions before analysing the fluctua-

tions (Miville-Deschênes, Joncas, & Durand 1995; Lagrois & Joncas 2011), whereas others analyse the unfiltered observations (O’Dell & Wen 1992; Medina Tanco et al. 1997). Also, in some cases multiple Gaussian velocity components are fitted to the line profiles (Castañeda 1988; Wen & O’Dell 1993), which are then assigned to a small number of velocity “systems” that are each analysed separately, whereas in most studies the mean velocity of the entire line profile is used.

Despite these differences, there are interesting commonalities in the results: a rising structure function with  $m_{2D} = 0.5\text{--}1.0$  is nearly always found at the smallest scales, which transitions to a flat structure function with  $m_{2D} \sim 0$  at larger scales. However, the scale at which the transition occurs varies enormously from object to object, from 0.02–0.2 pc in compact ( $R = 1$  to 5 pc) Galactic H II regions (O’Dell, Townsley, & Castañeda 1987; Castañeda 1988; Wen & O’Dell 1993; Miville-Deschênes, Joncas, & Durand 1995), up to 50 pc in giant ( $R \sim 400$  pc) extragalactic regions (Lagrois & Joncas 2011). We comment that the sound-crossing time for a region of size 50 pc is about 5 Myr, roughly the same as the estimated age of the NGC 595 nebula (Drissen, Moffat, & Shara 1990). For the full extent of NGC 595, the sound crossing time is about 40 Myr. It is therefore unlikely that the turbulence in such large regions is in a statistically steady state unless it is highly supersonic. Indeed, O’Dell & Townsley (1988) suggest that in the case of large extragalactic H II regions, the large linewidths could be due to multiple velocity components, that is, regions of the H II region separated by more than a sound-crossing time are kinematically distinct. Such giant H II regions show velocity centroid dis-

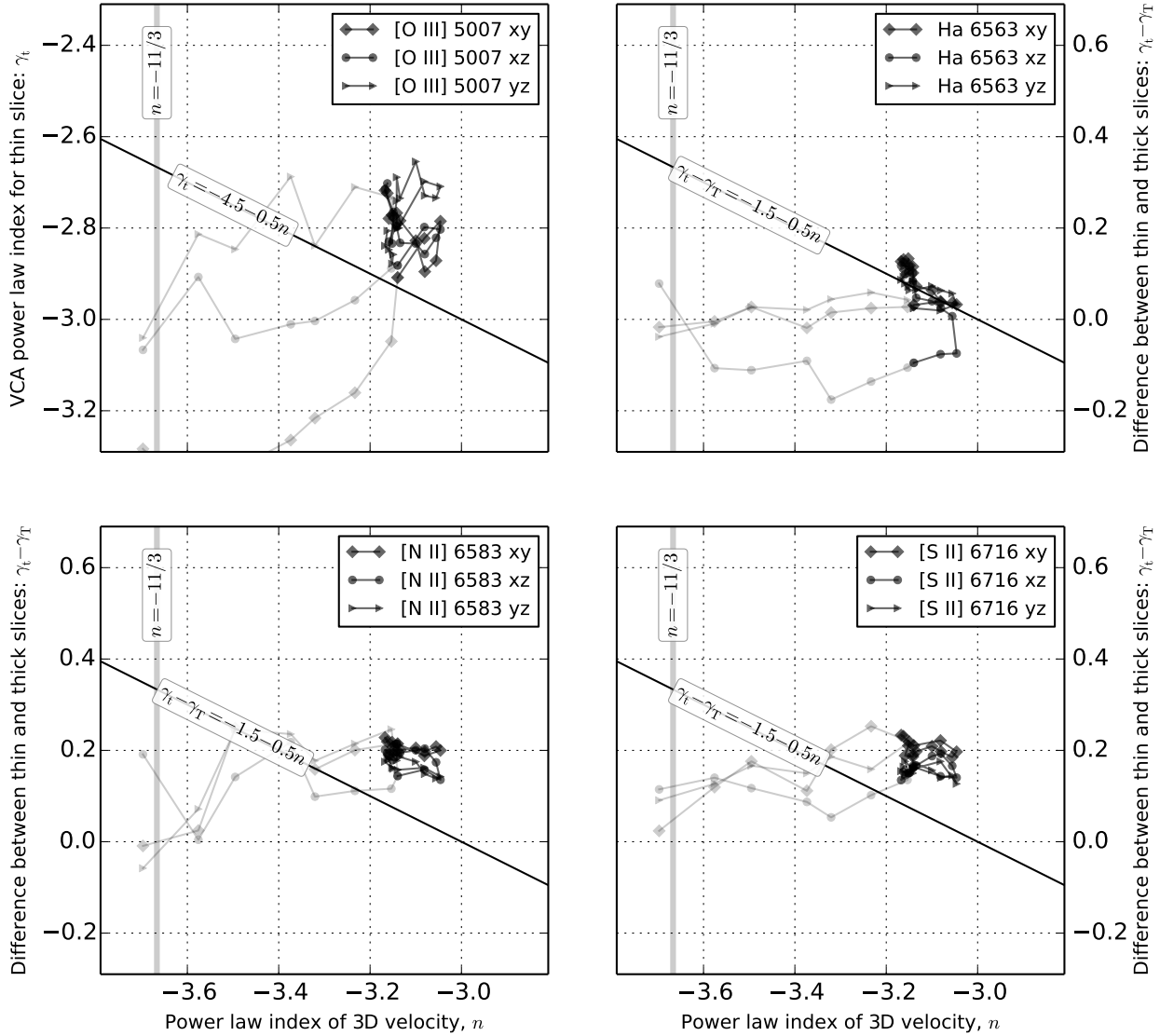


**Figure 11.** As Fig. 9, but showing VCA power spectrum slopes for thin slices,  $\gamma_t$  or  $\gamma_t - \gamma_T$ , versus slope,  $n$ , of the intrinsic velocity power spectrum for each emission line. The [O III] line (upper left panel) has a sufficiently steep emissivity power spectrum that it is the absolute value of  $\gamma_t$  that is predicted to be related to  $n$ , as shown by the diagonal solid line. The other emission lines have a shallower emissivity power spectrum, such that it is the relative slope between the thin and thick slices,  $\gamma_t - \gamma_T$  that is predicted to depend on  $n$ .

persions of  $\sigma_c > 10 \text{ km s}^{-1}$  on the largest scales, which is several times larger than is seen in compact single-star regions or in our simulations. We will therefore not consider them further since they are governed by additional physical processes, such as powerful stellar winds and the cluster gravitational potential, which are beyond the scope of the current paper.

The explanations that have been offered for the break in the structure function slope are also varied. In the case of compact H II regions, it is often taken to indicate the characteristic line-of-sight depth of the emission zone (von Hoerner 1951; O'Dell & Castañeda 1987), with projection smoothing steepening the slope at the smaller separations (see § 2.3.4 above). If that were the case, then the correct three-dimensional structure function slope is the flat one:

$m_{3D} \sim 0$ , corresponding to a velocity power spectrum slope of  $n = -3$ . This interpretation would be broadly consistent with our simulation results, which show a very similar velocity power spectrum (Fig. 3). However, our simulated structure functions rarely show a clear break in the same way as the observations do, although they do show a slight negative curvature in many cases. This is probably because of the very limited useful dynamic range, roughly a factor of 10, that the simulations allow between the small scales that are affected by numerical diffusion and the large scales, that are affected by systematic flows, anisotropies, and edge-effects.

An alternative explanation for the observed break in the structure function is that it represents the scale of the largest turbulent eddies (Castañeda 1988; Miville-Deschênes, Jon-

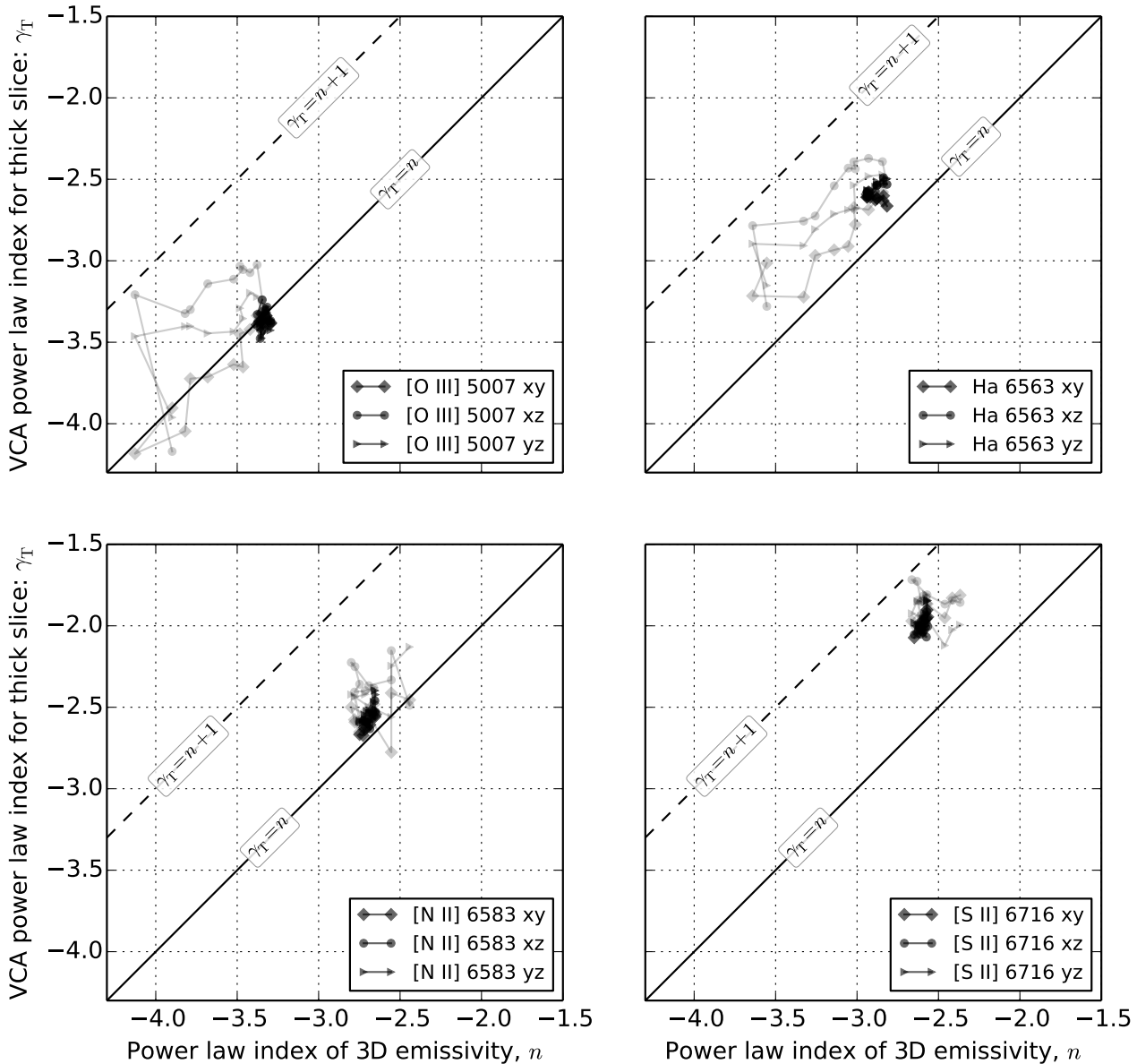


**Figure 12.** As Fig. 9, but showing VCA power spectrum slopes for thick slices,  $\gamma_T$ , versus slope,  $n$ , of the intrinsic emissivity power spectrum for each emission line. The theoretical expectations are shown by diagonal lines for the cases where the line-of-sight depth of the emitting region is larger (continuous line) or smaller (dashed line) than the transverse scales that are sampled.

cas, & Durand 1995) and that the fluctuations at larger scales are simply uncorrelated. In such a picture it would still be necessary to postulate a velocity spectrum considerably shallower than Kolmogorov in order to explain the small-scale slope.

Based on the discussion of our simulation results above (§ 4.1.3), it seems that Velocity Channel Analysis would be a very useful complement to the structure function, since it is less affected by uncertainties in projection smoothing and gives a more consistent result between different emission lines (at least, for our simulations).

In a forthcoming paper, we will present such an analysis of recent high-resolution echelle spectroscopy of multiple

emission lines in the Orion Nebula (García-Díaz et al. 2008; O’Dell & Henney 2008).

## 5 SUMMARY

(i) We have investigated the statistics of fluctuations in physical conditions within a radiation-hydrodynamic simulation of the evolution of an H II region inside a highly inhomogeneous molecular cloud. We find that steady-state turbulence, corresponding to time-independent profiles of the 3D power spectra, is only established after about 1.5 sound-crossing times of the H II region. In these simulations, this corresponds to about 200,000 years (§ 3.2.1).



(ii) We find a power-law behaviour for the 3D power spectra in the range from about 1 pc down to 0.125 pc, equivalent to 16 computational cells. The larger scale can be interpreted as the size of the largest photoevaporated flows, while the smaller scale is about twice the numerical dissipation scale. The power-spectrum slopes of the velocity and density fluctuations are very similar and always lie in the range  $-3.1 \pm 0.1$ . This is significantly shallower than the slope predicted for the inertial range of either incompressible or compressible turbulence ( $-3.667$  to  $-4.1$ ). This suggests that turbulent driving is occurring over all scales in our simulation, unlike the case of classical turbulence where energy is injected only at the largest scales. The power-spectrum slopes of the emissivities of optical lines are even shallower, increasingly so for lower ionization lines, indicating that the smallest scale fluctuations are dominant (§ 4.1.1).

(iii) We investigate in detail the utility of observational diagnostics for inferring the power spectra of emissivity and velocity fluctuations in our simulation. We find that the traditional velocity centroid structure function technique gives ambivalent results because of the effects of projection smoothing, combined with the fact that the effective line-of-sight depth of the emitting gas does not have a single well-defined value. In addition, the presence of anisotropic motions such as champagne flows can yield misleading structure function slopes when the simulation is viewed from certain directions (§ 4.1.2).

(iv) The more recently developed technique of Velocity Channel Analysis is found to offer a more robust diagnostic of the three-dimensional velocity statistics of our simulation. The slope of the velocity power spectrum can be correctly recovered to a precision of  $\pm 0.1$  from either high or low ionization lines, and with no significant dependence on viewing direction (§ 4.1.3).

## ACKNOWLEDGMENTS

**SNXM** acknowledges a CONACyT, Mexico student fellowship. SJA would like to thank DGAPA-UNAM for financial support through project IN101713. SJA, WJH and GM thank Nordita for support during the program Photo-Evaporation in Astrophysical Systems.

## REFERENCES

- Arthur S. J., Henney W. J., Mellema G., de Colle F., Vázquez-Semadeni E., 2011, *MNRAS*, 414, 1747
- Beckman J. E., Relaño M., 2004, *Ap&SS*, 292, 111
- Boldyrev S., Nordlund Å., Padoan P., 2002, *ApJ*, 573, 678
- Brunt C. M., Federrath C., Price D. J., 2010, *MNRAS*, 405, L56
- Brunt C. M., Heyer M. H., 2002, *ApJ*, 566, 276
- Brunt C. M., Heyer M. H., Vázquez-Semadeni E., Pichardo B., 2003, *ApJ*, 595, 824
- Brunt C. M., Mac Low M.-M., 2004, *ApJ*, 604, 196
- Burgers J. M., 1974, *The Nonlinear Diffusion Equation* (Dordrecht: Reidel)
- Castañeda H. O., 1988, *ApJS*, 67, 93
- Castañeda H. O., O'Dell C. R., 1987, *ApJ*, 315, L55
- Chandrasekhar S., 1949, *ApJ*, 110, 329
- Dickman R. L., Kleiner S. C., 1985, *ApJ*, 295, 479
- Drissen L., Moffat A. F. J., Shara M. M., 1990, *ApJ*, 364, 496
- Dyson J. E., 1968, *Ap&SS*, 1, 388
- Esquivel A., Lazarian A., 2005, *ApJ*, 631, 320
- Esquivel A., Lazarian A., Horibe S., Cho J., Ossenkopf V., Stutzki J., 2007, *MNRAS*, 381, 1733
- Esquivel A., Lazarian A., Pogosyan D., Cho J., 2003, *MNRAS*, 342, 325
- Eulderink F., Mellema G., 1995, *A&AS*, 110, 587
- Federrath C., 2013, *MNRAS*, 436, 1245
- Federrath C., Roman-Duval J., Klessen R. S., Schmidt W., Mac Low M.-M., 2010, *A&A*, 512, A81
- Galtier S., Banerjee S., 2011, *PhRvL*, 107, 134501
- García-Díaz M. T., Henney W. J., 2007, *AJ*, 133, 952
- García-Díaz M. T., Henney W. J., López J. A., Doi T., 2008, *RMxAA*, 44, 181
- García-Segura G., Franco J., 1996, *ApJ*, 469, 171
- Henney W. J., 2003, *RMxAC*, 15, 175
- Henney W. J., Arthur S. J., de Colle F., Mellema G., 2009, *MNRAS*, 398, 157
- Kleiner S. C., Dickman R. L., 1985, *ApJ*, 295, 466
- Kolmogorov A., 1941, *DoSSR*, 30, 301
- Kritsuk A. G., Norman M. L., Padoan P., Wagner R., 2007, *ApJ*, 665, 416
- Lagrois D., Joncas G., 2011, *MNRAS*, 413, 721
- Lagrois D., Joncas G., Drissen L., Arsenault R., 2011, *MNRAS*, 413, 705
- Lazarian A., Pogosyan D., 2000, *ApJ*, 537, 720
- Mackey J., Lim A. J., 2010, *MNRAS*, 403, 714
- Medina Tanco G. A., Sabalisk N., Jatenco-Pereira V., Opher R., 1997, *ApJ*, 487, 163
- Mellema G., Arthur S. J., Henney W. J., Iliev I. T., Shapiro P. R., 2006, *ApJ*, 647, 397
- Mellema G., Iliev I. T., Alvarez M. A., Shapiro P. R., 2006, *NewA*, 11, 374
- Miville-Deschênes M.-A., Joncas G., Durand D., 1995, *ApJ*, 454, 316
- Miville-Deschênes M.-A., Levrier F., Falgarone E., 2003, *ApJ*, 593, 831
- Münch G., 1958, *RvMP*, 30, 1035
- O'Dell C. R., 1986, *ApJ*, 304, 767
- O'Dell C. R., Castañeda H. O., 1987, *ApJ*, 317, 686
- O'Dell C. R., Henney W. J., 2008, *AJ*, 136, 1566
- O'Dell C. R., Townsley L. K., 1988, *A&A*, 198, 283
- O'Dell C. R., Townsley L. K., Castañeda H. O., 1987, *ApJ*, 317, 676
- O'Dell C. R., Wen Z., 1992, *ApJ*, 387, 229
- Osterbrock D. E., Ferland G. J., 2006, *Astrophysics of gaseous nebulae and active galactic nuclei*, 2nd. ed. Sausalito, CA: University Science Books
- Porter D., Pouquet A., Woodward P., 2002, *PhRvE*, 66, 026301
- Roy J.-R., Joncas G., 1985, *ApJ*, 288, 142
- She Z.-S., Leveque E., 1994, *PhRvL*, 72, 336
- Spitzer L., 1978, *Physical Processes in the Interstellar Medium* (New York: Wiley-Interscience)
- Stutzki J., Bensch F., Heithausen A., Ossenkopf V., Zielinsky M., 1998, *A&A*, 336, 697
- Sutherland R. S., Bisset D. K., Bicknell G. V., 2003, *ApJS*, 147, 187

- Vázquez-Semadeni E., Kim J., Ballesteros-Paredes J., 2005, *ApJ*, 630, L49  
 von Hoerner S., 1951, *ZA*, 30, 17  
 Wen Z., O'Dell C. R., 1993, *ApJ*, 409, 262  
 Williams R. J. R., Ward-Thompson D., Whitworth A. P., 2001, *MNRAS*, 327, 788

## APPENDIX A: EXAMPLE SECOND-ORDER STRUCTURE FUNCTIONS OF THE LINE-OF-SIGHT VELOCITY CENTROIDS

Figures A1 to A3 show the second-order structure functions of the line-of-sight velocity centroid maps (see §§ 4.1.2 and 2.3.2) for the four emission lines at the four evolutionary times depicted in Figure 1. If turbulence is present, the second-order structure function should exhibit an inertial range over which it is a power law with length scale. Accordingly, we perform a least-squares fit to the data points. However, it is not immediately clear what the limits for the fit should be.

At small scales, the lower limit for the inertial range should be defined by the scale at which numerical dissipation effects cease to be important (Brunt & Mac Low 2004). For the present simulations, we tested several values and the size scale equivalent to 10 computational cells proved to be adequate for all emission lines and evolution times studied. For the upper limit, we examined the projected emission maps and calculated the area occupied by the pixels having greater than the mean intensity. This method is independent of the resolution of the image and could equally be applied to images obtained from observations. We then took the radius of the circle having the same area to be the upper limit for the least-squares fit. This procedure appears to work very well, as can be seen in Figures A1 and A3. If a different line of sight is chosen, the radius of this circle will be different and needs to be calculated self-consistently for every projection. Note that the inertial range for each combination of line and view tends to become broader with time due to the expansion of the H II region. At the latest time, 300,000 yrs, both the H $\alpha$  and [O III] $\lambda$ 5007 structure functions appear to develop a break, which would be better fit by two power laws, one below a scale of about 0.3 pc and a steeper one for larger scales. However, we have fit just a single power law to both of these cases. We speculate that this apparent break in the power law at late times could be due to energy injection at size scales associated with the photoevaporated flows emanating from the ubiquitous clumps and filaments seen in the emission-line images (see Fig. 1).

An alternative criterion for the upper limit was used by Lagrois & Joncas (2011) who used the theoretical result for isotropic, homogeneous turbulence that decorrelation of the second-order structure function occurs when the auto-correlation function changes sign from positive to negative. In the theory, this corresponds to the scale for which the second-order structure function is equal to 2. Figure A4 shows the structure function and auto-correlation function obtained from our simulations at times 150,000 yrs and 250,000 yrs for the [O III] $\lambda$ 5007 emission line velocity centroids projected onto the  $yz$ -plane. The other emission lines and viewing directions give very similar results. From this figure, we see that at early times, when the structure func-

tion does indeed rise above 2, this corresponds approximately to the length scale at which the auto-correlation function changes sign. However, at later times the auto-correlation function changes sign at a length scale much smaller than the size of the computational box but the structure function remains less than 2. This suggests that the assumptions of the simple theory (isotropic, homogeneous turbulence) do not apply to the emission-line velocity centroids obtained from our simulations. Figure A4 also indicates the fitting range suggested by the procedure described earlier. At early times, our procedure results in a slightly larger upper length scale for the power-law fit than using the zero point of the auto-correlation function. At later times, the two more-or-less coincide and this is true for all the emission lines, viewing angles and times we have examined. Since there is no clear reason to prefer the auto-correlation approach, we will use our computationally simpler procedure to determine the upper length scale for the power-law fit.

## APPENDIX B: EXAMPLE POWER SPECTRA FROM VELOCITY CHANNEL ANALYSIS

Figures B1 to B3 show the power spectra resulting from the velocity channel analysis (see § 2.3.3). Each of the three figures is for a different viewing direction and shows the four emission lines at four different times. For each combination of line and time, there are two panels: an upper panel without including thermal Doppler broadening and a lower panel with the broadening effects included. In each graph, two power spectra are plotted: one representing a very thick velocity slice (i.e., encompassing all the emission) and the other averaged over thin velocity slices of width  $\delta v \sim 5 \text{ km s}^{-1}$ . Also shown are the least-squares power-law fits to the thin and very thick slice spectra and the range in wavenumber over which the fit is calculated. This wavenumber range corresponds to the length-scale range used for the structure function fits (see § 3.2.2). The very thick velocity slice is equivalent to the total intensity along the line of sight and its power spectrum does not vary with the addition of thermal broadening.

It is clear that the thermal broadening has a large effect on the VCA of the H $\alpha$  line, effectively erasing the difference in slope between the thin and thick slices. For photoionized gas at  $T_e = 10^4 \text{ K}$ , the FWHM of the H $\alpha$  line is  $\sim 22 \text{ km s}^{-1}$ , while that of an oxygen line is a quarter of this,  $\sim 5.5 \text{ km s}^{-1}$ . Indeed, the heavier ions are less affected by thermal broadening, but a slight steepening of the thin-slice power spectra can still be seen, amounting to a reduction in  $\gamma_t$  of  $\sim 0.1$ .

For the thermally broadened case, the variation with time of the slopes of these fits,  $\gamma_T$  for the thick slices and  $\gamma_t$  for the thin slices, is shown in Fig 8 and discussed in § 3.2.3.

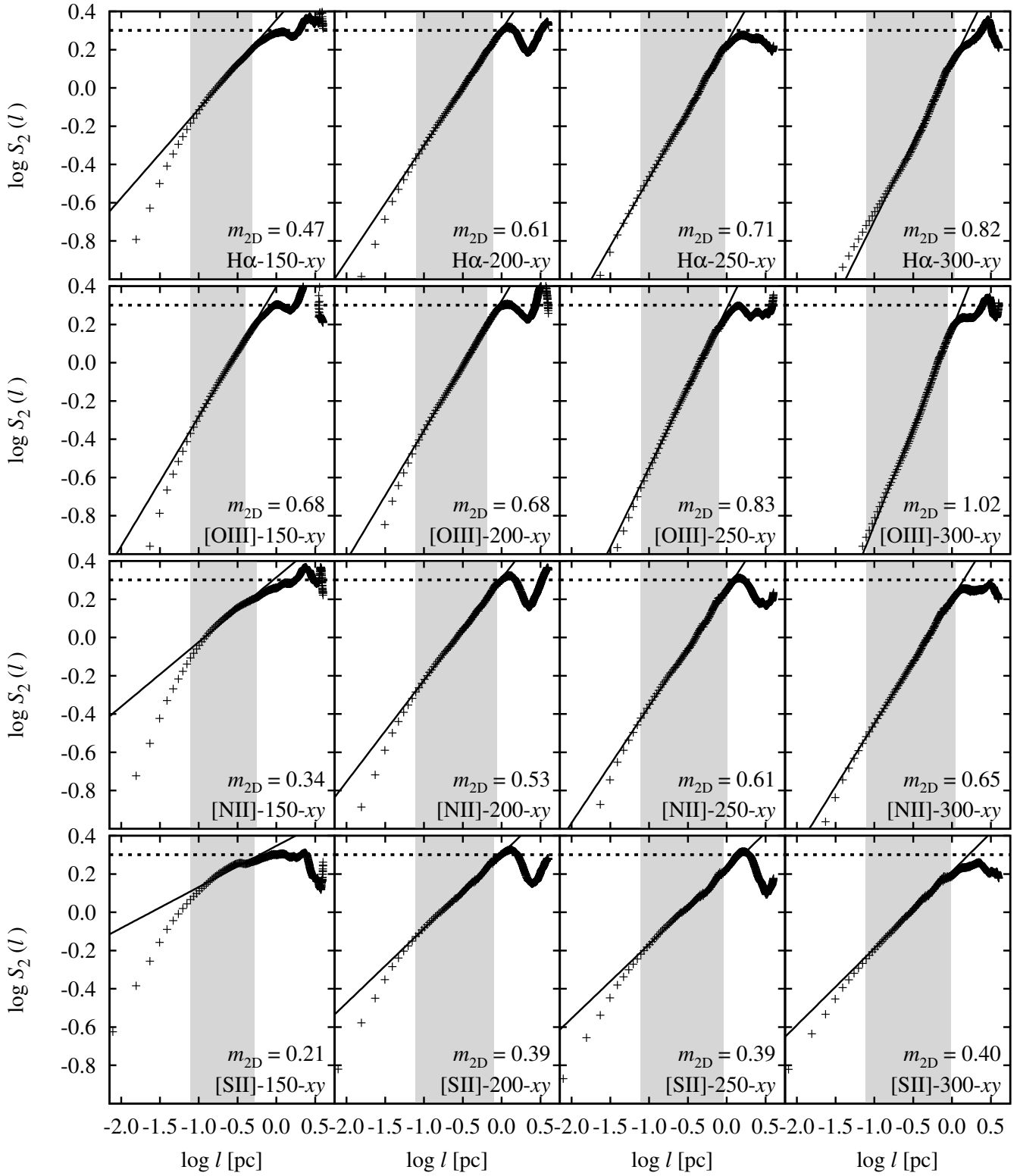


**Figure A1.** Second-order structure functions against length scale for projection onto the  $xy$ -plane. From top to bottom:  $H\alpha$ ,  $[O\text{ III}]\lambda 5007$ ,  $[N\text{ II}]\lambda 6584$ ,  $[S\text{ II}]\lambda 6716$ . From left to right: 150,000, 200,000, 250,000 and 300,000 years. The points represent the calculated structure function for the numerical simulation. The solid line is the least-squares fit to the data points between limits described in the text, represented by the grey rectangle. The horizontal dotted line at  $\log S_2(l) = 2$  is included as a reference value.

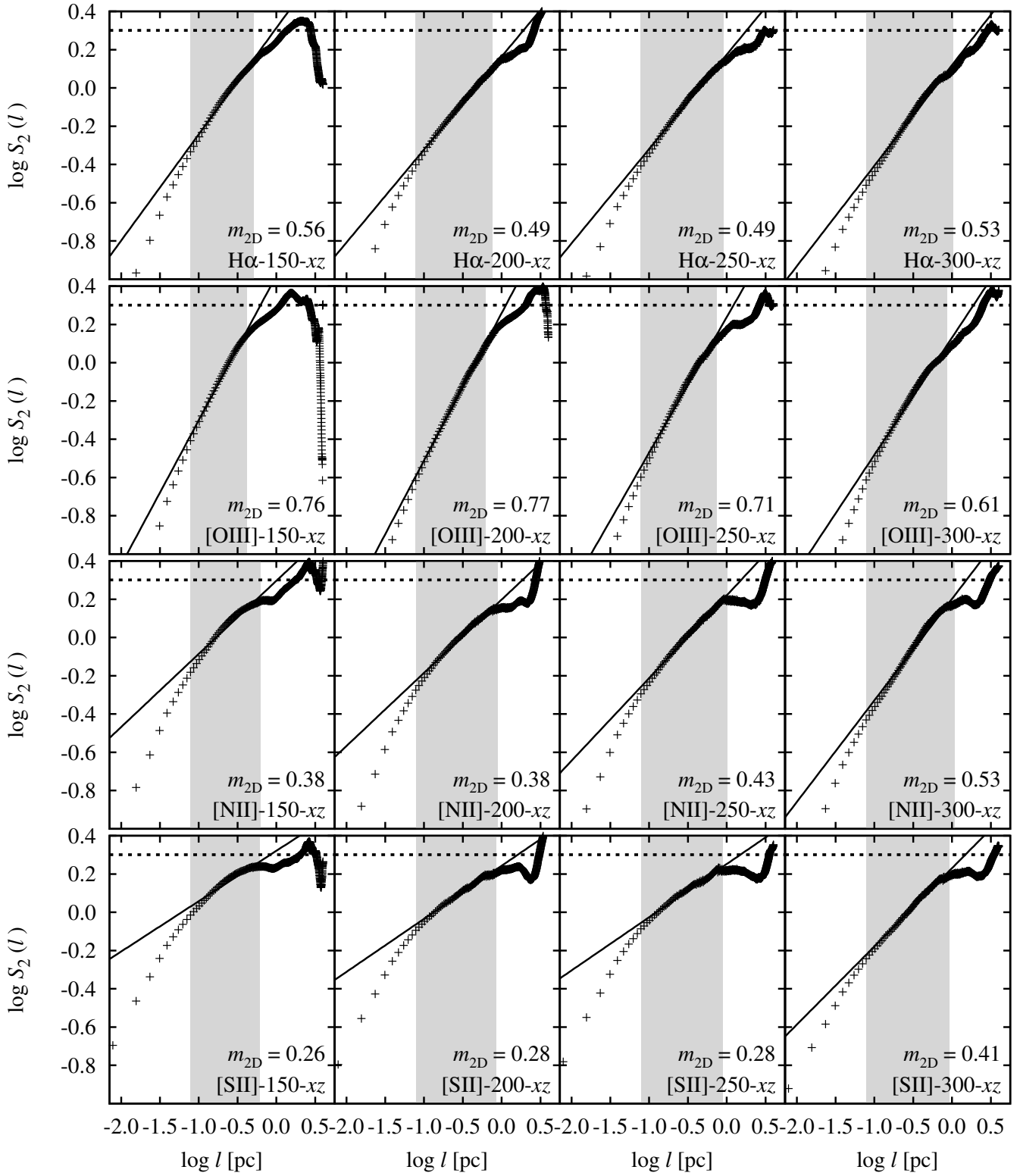
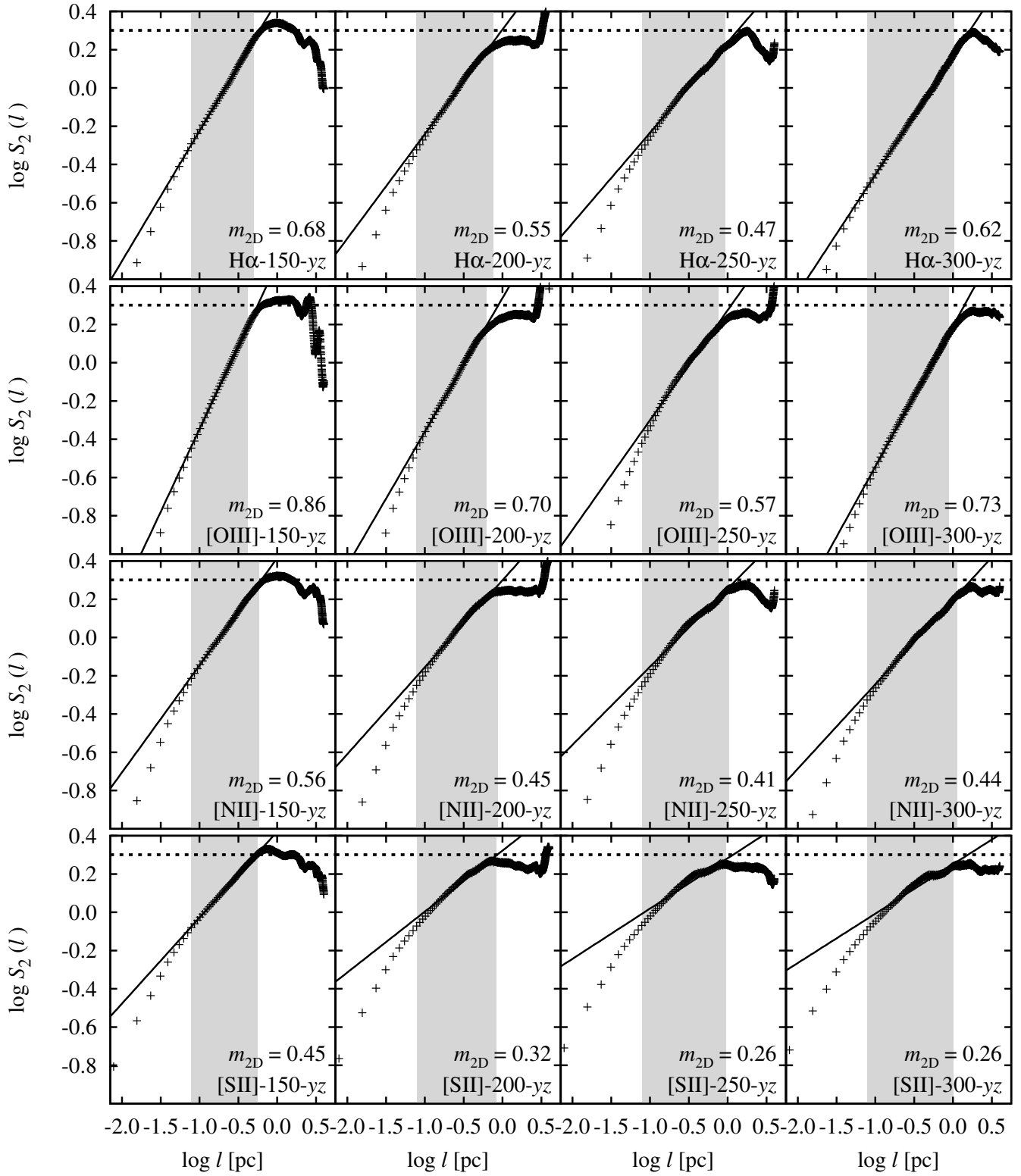
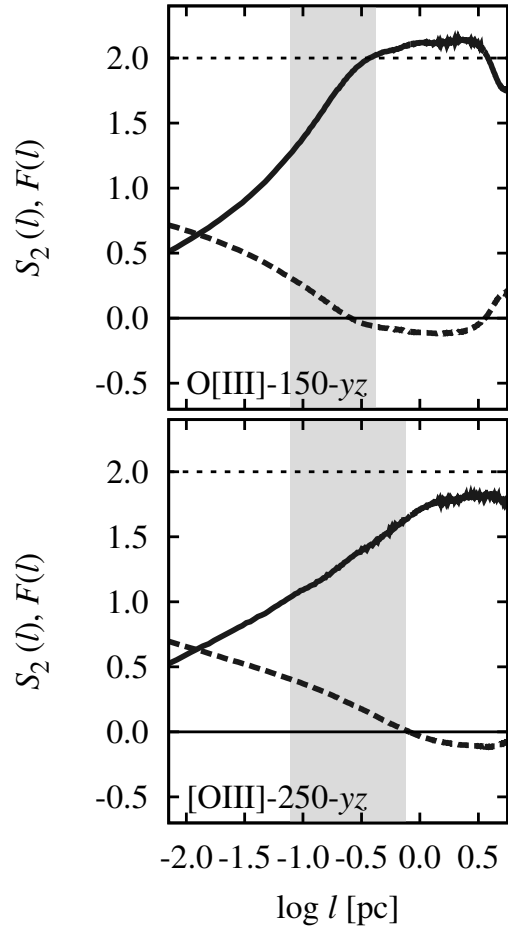


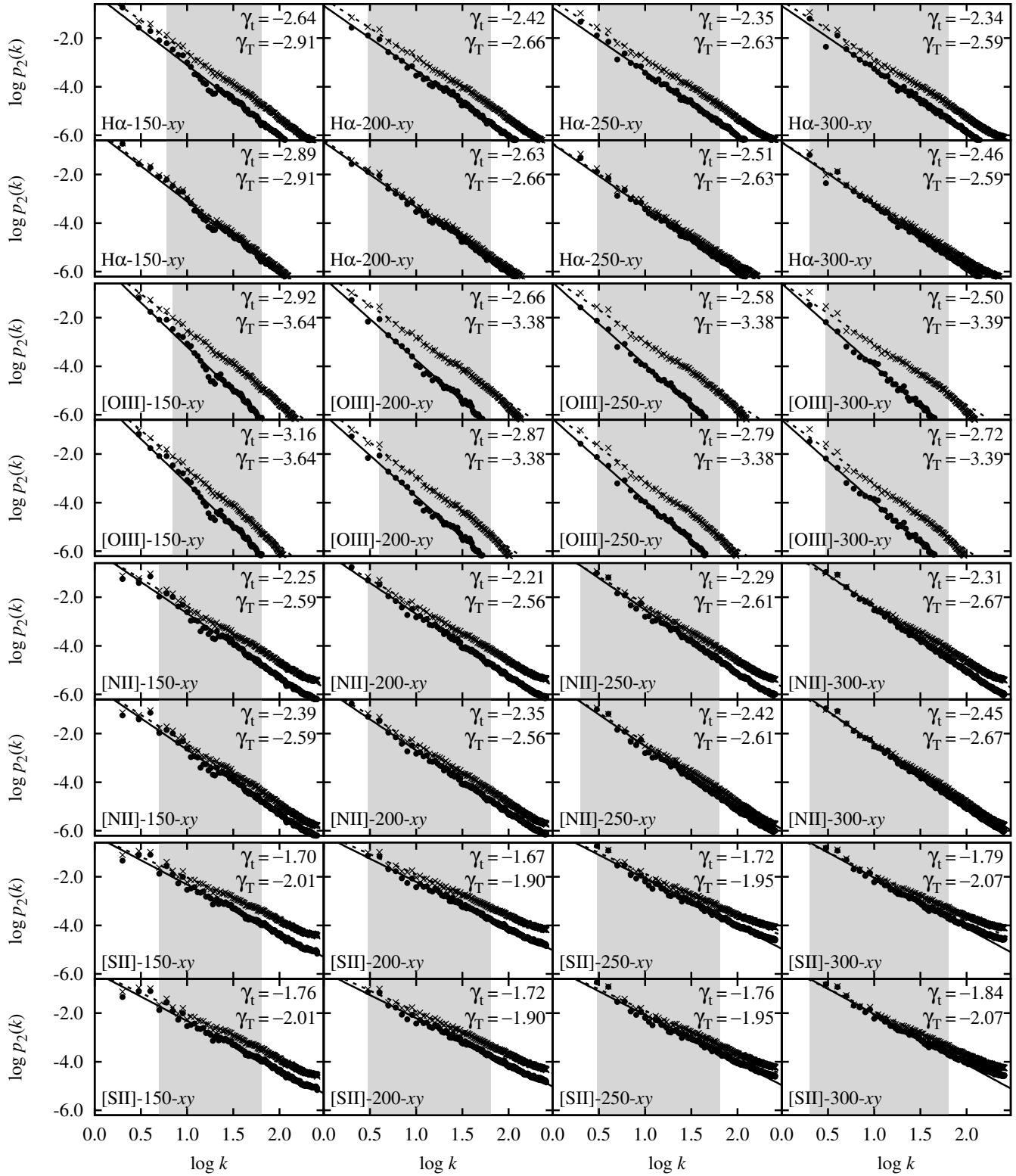
Figure A2. Same as Fig. A1 but for a projection onto the  $xz$  plane.



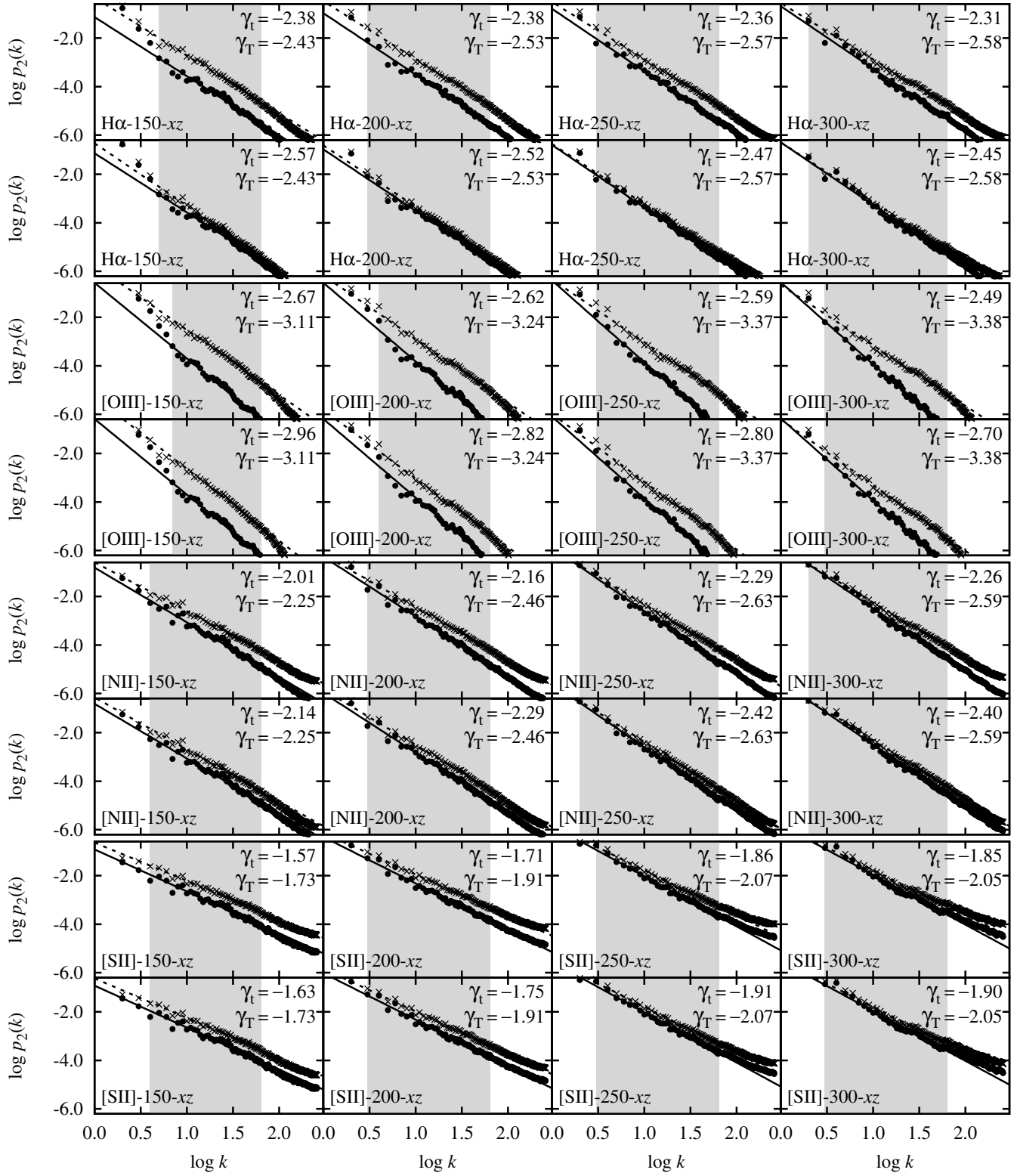
Figure A3. Same as Fig. A1 but for a projection onto the  $yz$ -plane.



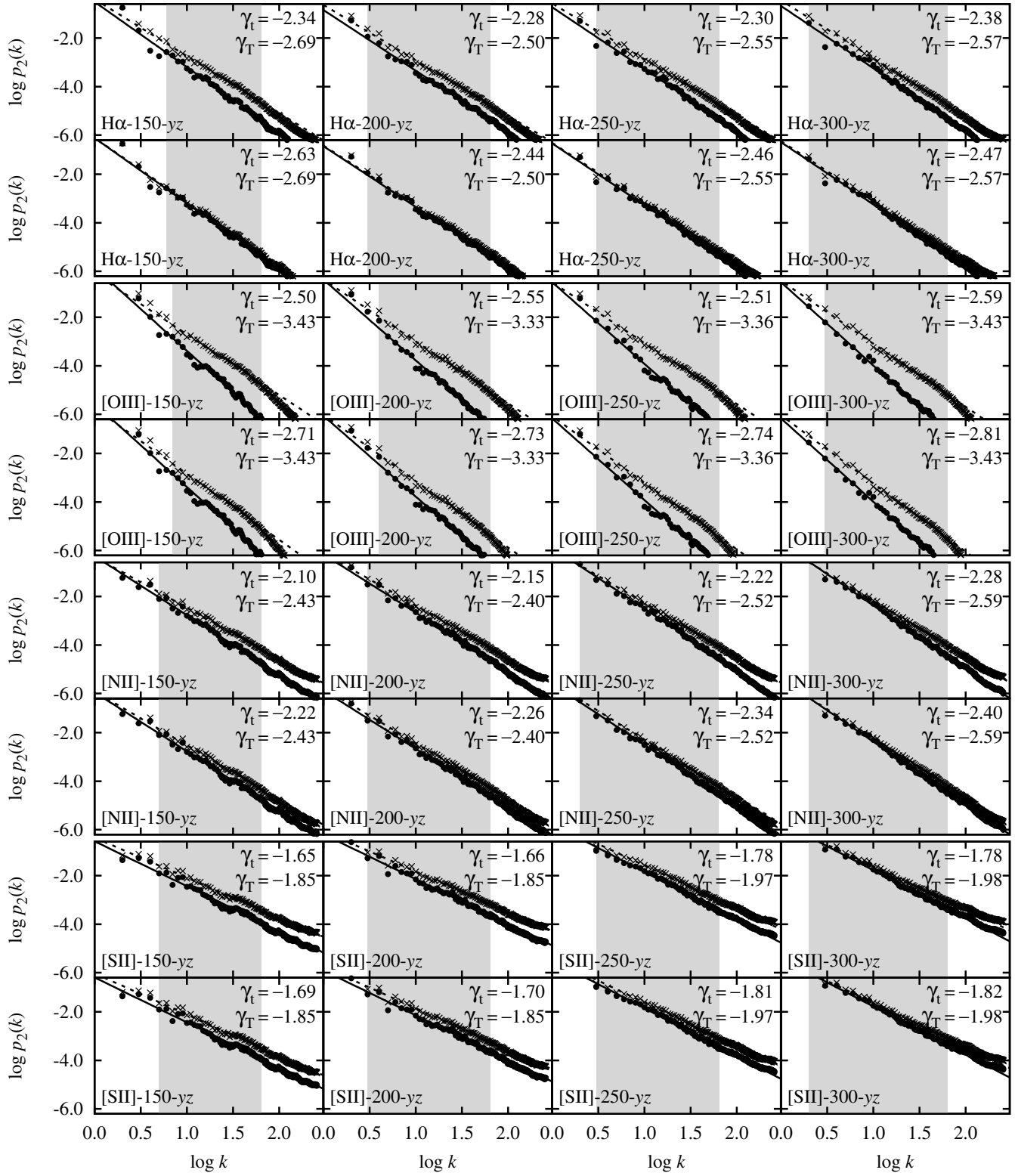
**Figure A4.** Second-order structure function (thick solid line) and auto-correlation function (thick dashed line) against logarithmic length scale. The horizontal lines at 2 and 0 are included as reference values.



**Figure B1.** Power spectra of the velocity channels. From top to bottom: H $\alpha$ , [O III] $\lambda$ 5007, [N II] $\lambda$ 6584, [S II] $\lambda$ 6716. From left to right: 150,000, 200,000, 250,000 and 300,000 years. The upper panel in each figure are for velocities without thermal broadening, the lower panel is the case with thermal broadening. The points represent the calculated power spectra for the numerical simulation: Crosses—thin slice ( $n = 32$  channels), filled circles—thick slice ( $n = 1$  channel). The dashed line is the least-squares fit to the data points for the thin slice between limits described in the text represented by the grey rectangle. The solid line is the least-squares fit to the data points for the thick slice.

Figure B2. Same as Fig. B1 but for a projection onto the  $xz$  plane.



Figure B3. Same as Fig. B1 but for a projection onto the  $yz$ -plane.